

Highlights

Experimental and LES investigation of ignition of a real high energy aeroengine igniter under relevant operating conditions

Javier Crespo-Anadon, Carlos J Benito-Parejo, Stéphane Richard, Eleonore Riber, Bénédicte Cuenot, Camille Strozzi, Julien Sotton, Marc Bellenoue

- First presentation of the Radius chamber ignition test rig and measurements.
- Large-Eddy Simulations with semi-detailed chemistry describing the first instants of ignition and flame propagation; validation by comparison with experiments.
- Impact of two formulations (static and dynamic) for the subgrid closure of chemistry-turbulence interaction on the flame-propagation.

Experimental and LES investigation of ignition of a real high energy aeroengine igniter under relevant operating conditions

Javier Crespo-Anadon^{a,b}, Carlos J Benito-Parejo^c, Stéphane Richard^a, Eleonore Riber^b, Bénédicte Cuenot^b, Camille Strozzi^c, Julien Sotton^c, Marc Bellenoue^c

^a*SAFRAN Helicopter Engines, Avenue Joseph Szydlowski, Bordes, 64510, France*

^b*CERFACS, 42 Avenue Gaspard Coriolis, Toulouse, 31100, France*

^c*Institut P', 11 Boulevard Marie et Pierre Curie, Poitiers, 86073, France*

Abstract

SAFRAN Helicopter Engines has developed the spinning combustion technology in which the burnt gases from one injector travel tangentially along the combustor annulus towards the neighboring injectors. Compared to a conventional design, this arrangement modifies the ignition process, which is a critical phase for aeroengines. In order to understand the ignition process in this technology, experiments and Large-Eddy Simulation (LES) have been performed in a cylindrical combustion chamber where the flow is injected tangentially (named Radius chamber). Three cases are considered with different strain and turbulence levels representative of real combustor flows. Micro calorimetry and the Background-Oriented Schlieren technique allows for detailed temporal measurements of energy deposited in the flame kernel. Pressure measurement and Schlieren imaging are used to study the flame propagation. LES are performed with a 19-species and 184-reactions analytically-reduced chemistry together with the thickened flame approach allowing the description of the first instants of ignition in a quasi-DNS mode and ensuing flame propagation. Both a static and dynamic formulations of the efficiency function to describe sub-grid scale chemistry-turbulence interaction are used. Results show that LES is able to capture the flame kernel formation and trajectory as well as the time to reach maximum pressure within an error of 10% when using a dynamic formulation. On the other hand, the static formulation of the efficiency function predicts the time for maximum pressure within a maximum error of 20%.

Keywords: Ignition, Analytically Reduced Chemistry, LES, Spinning combustion technology

1. Introduction

A great challenge in aeronautical combustors consists in ensuring ignition at all flight conditions, in particular at high altitude where low temperature and pressure make ignition more difficult. Safran HE has recently developed the spinning combustion technology (SCT) depicted in Fig. 1. It consists in injecting the airflow and the fuel tangentially into the combustor. In this way, the hot gases produced by the flame attached to one injector are directed towards the next injector along the combustor annulus, eventually creating a unique flame ring which expands across the full combustor.

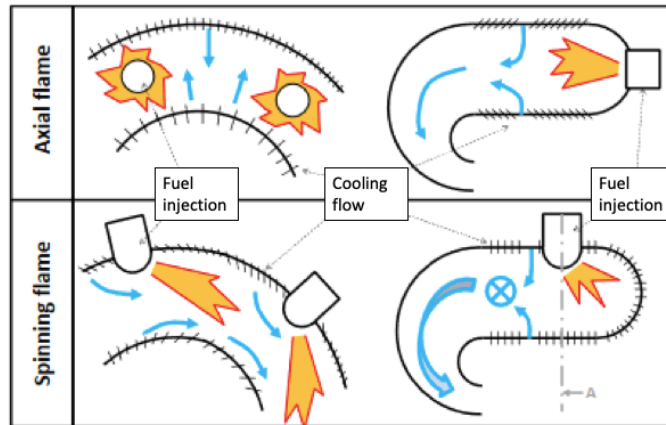


Figure 1: Spinning combustion technology (SCT) adapted from [1]

This technology has several advantages, among which it offers better igniting capability, which can be beneficial for future hybrid-electric systems, greater temperature homogeneity at the combustor exit, and reduced mass and cost.

Despite recent insights gained into ignition in conventional aeroengine designs [2, 3, 4], specific work is required for SCT, which introduces new mechanisms. Recent research [5, 6] indicate that the ignition kernel evolution is independent of the first instants just after sparking, thus reducing the need for a detailed description until times after spark $O(10\mu s)$. After the kernel is formed, ignition success depends on the chemical heat release

rate overcoming the rate of heat diffusion. Only large enough kernels can sustain these conditions. The success in this phase is usually studied by the concept of minimum ignition energy (MIE) which is the value of energy that allows for 50% of probability of successful ignition [7]. The stochastic character of ignition mainly originates from turbulence inducing mixture fraction fluctuations [8], and velocity fluctuations at the spark location [9].

The MIE depends on several factors [3]:

- Igniter parameters: The electrode geometry and the temporal power supply distribution control the spatial distribution and intensity of the deposited energy.
- Gas-phase parameters: The mean and fluctuating flows have a direct impact through mixing while local conditions may favor or disadvantage chemical activity. This effect is illustrated in Fig. 2
- Liquid-fuel parameters: Volatility and spray characteristics such as droplet density and size distribution are of primary importance for the vapor distribution.

The effect of turbulence on the early flame structure depends on the relative size of the eddies to the kernel [10], which may be evaluated with the ratios u'/S_L and L/d_k where u' is the velocity fluctuation, S_L the laminar flame speed, L a turbulent scale and d_k the kernel size. If the kernel is small compared to the turbulent scales, it is only convected by eddies. When the kernel grows, vortices start to interact with the flame [11]. Fast chemistry will allow the kernel to resist and be only wrinkled by the eddies. Conversely, if chemistry is too slow, the kernel may locally quench and break into smaller parts. These effects are summarized in Fig. 3.

Measurements of quenching distance (d_q), defined as the minimum radius for a flame kernel to lead to successful ignition, are available for different pressures, turbulence intensities, turbulence scales and equivalence ratios. The following dependencies were found for gaseous mixtures at several turbulence levels [12] with λ , ρ , c_p being respectively the heat conductivity, density and specific heat at constant pressure:

$$d_q = \frac{\frac{10\lambda}{c_p\rho}}{S_L - 0.63u'} \quad \text{for } u' \leq 2S_L$$

$$d_q = \frac{\frac{10\lambda}{c_p\rho}}{S_L - 0.16u'} \quad \text{for } u' > 2S_L$$
(1)

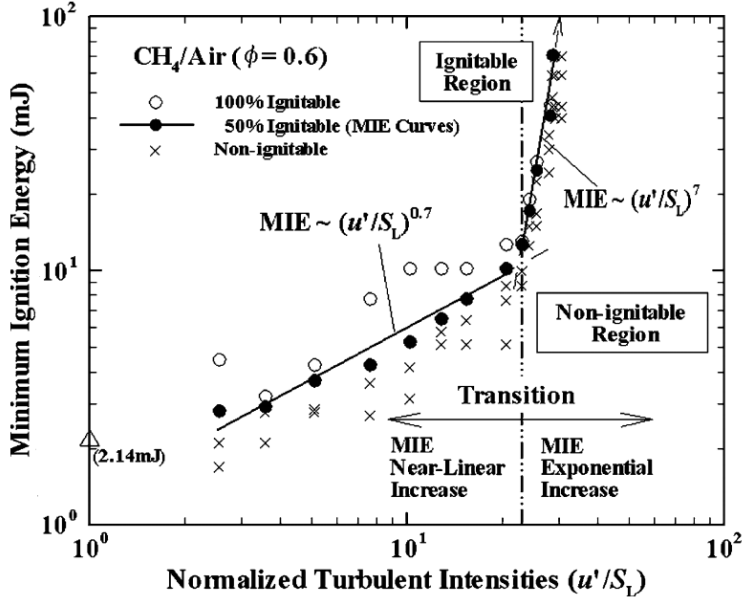


Figure 2: MIE of a uniform methane-air mixture in isotropic turbulence for different turbulent levels showing a change of behavior at $\frac{u'}{S_L} \approx 20$ [13]

The presence of the liquid phase further increases the MIE with respect to gaseous fuels due to the necessity to evaporate droplets [14, 15, 16, 12, 17].

After the kernel has grown to the size of the integral length scale, its evolution will depend on the conditions encountered during the flame propagation [18, 19]. Homogeneous conditions lead to the flame evolving as a premixed or stratified flame. On the other hand, large mixture fraction fluctuations may lead to local quenching and edge flame occurrence [2]. Some authors use the Karlovitz number to determine success of this stage [20] despite not being the only decisive parameter [2]. Flame stretch is another important parameter. Failure in this phase is related to the second mode or “long” failure mode discussed in [2].

If successful, flame propagation results in the flame stabilizing on an injector. Experiments [21, 22, 23] show that the flame must be trapped by the recirculation zone, have enough time to grow, and also be able to ignite the region near the anchoring point.

The final phase consists in the flame propagation between injectors until all injectors hold stable flames. The ratio of inter-injector space to swirler diameter affects the speed and the mode of flame propagation. In this phase, the azimuthal velocity and the combustor liner cooling flows are expected to

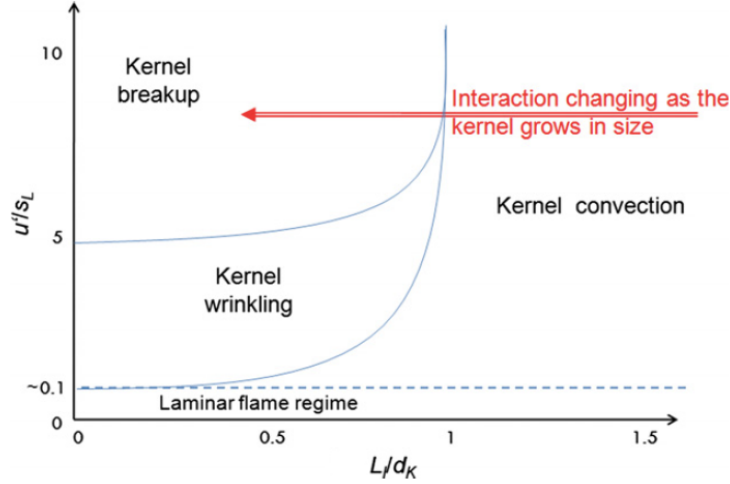


Figure 3: Turbulence regime map [10]

play an important role in the SCT.

The present study intends to give greater insight into the effect of turbulence and stretch levels on ignition in SCT under realistic engine conditions and strong swirling flow. For that purpose, an experimental configuration consisting of a closed chamber in which ignition occurs in a cross-flow has been developed and is described in section 2 together with available measurements. In section 3, the numerical modelling is described focusing on the modelling of chemistry kinetics and turbulent combustion. Finally, results from a static and a dynamic formulation of the turbulent combustion model are presented and discussed against experimental data.

2. The Radius test rig and available measurement

The experiment was carried out at PPRIME Institute in a constant volume vessel composed of a cylindrical chamber and equipped with a dynamic pressure gauge and optical access allowing pressure evolution measurements and high frequency visualization. Initially, the mixture of methane and air is stored at 6 bars in a tank, then it is tangentially injected through a gas injector into the initially empty chamber generating a swirling motion of the flow. The overall equivalence ratio is set to 0.7. The chamber is empty and it is filled by the mixture up to a pressure of 0.5 or 1 bar by varying injection

by a POM-C case. This rod connects the high voltage electrode to its coaxial cable. A mass cable connects the mass electrode to the coaxial cable corresponding part. The voltage signal applied to the Ardiden 3 igniter is measured with a Tektronix P6015A probe.

During electrical discharges, voltage and current variations occur in the order of tens of ns (in particular, hot plasma discharge breakdown voltage drops in tens of nanoseconds), so wideband electrical probes are required. The Tektronix P6015A is chosen as high voltage probe, with a 75 MHz bandwidth and measuring voltage peaks up to 40 kV. Concerning the current, the Pearson current monitor model 101 is used as high currents are expected with such igniter system, and it measures up to 50 kA with a 4 MHz bandwidth. Uncertainty for voltage and current are estimated to 3% and 1% respectively.



Figure 5: Adaptation to measure temporal current and voltage evolution

Finally, the temporal evolution of current and voltage (cf. a typical signal in Fig. 6) allows to determine the electrical power and the total electrical energy (see Fig. 7) delivered to the electrodes of the Ardiden 3 igniter. For this igniter, the overall electrical energy is around 625 mJ per discharge, with a maximum power peak of 13.5 kW.

2.2. Thermal Energy Released by the Ardiden 3 Igniter

The electrical energy determined by the current-voltage time evolution does not correspond to the thermal energy deposited into the fluid, which

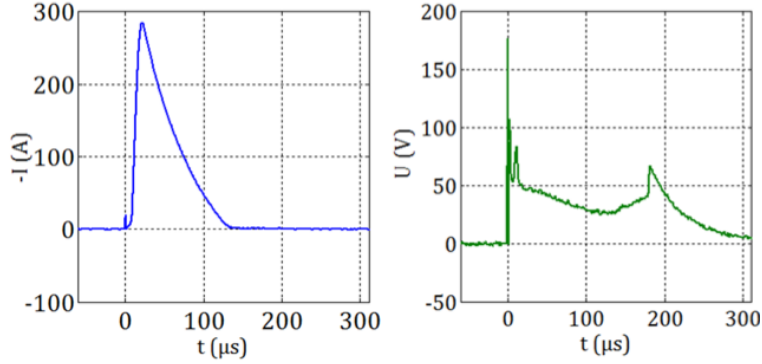


Figure 6: Typical electrical signals: Current (inversed, left) and Voltage (right).

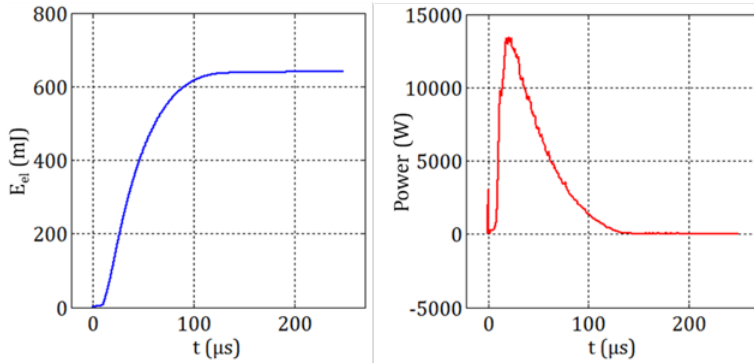


Figure 7: Typical electrical energy E_{el} (left) and electrical power (right).

is at the origin of the mixture ignition. For this objective, a calorimetry methodology is followed to characterize the energy release to the fluid, and thus determining the transmission efficiency of the ignition process.

The chosen calorimetry methodology consists in measuring the pressure increase induced by an electrical discharge in a closed vessel filled by inert gas at a given pressure. Considering the small volume of hot kernel compared to the chamber size, a single zone model can be used. As the pressure increase is small, a constant gas density is assumed, as well as an ideal gas behaviour. The thermal energy remaining into the gas after the discharge (E_{th}) is obtained from the pressure increase in the given chamber volume as:

$$E_{th} = \int_V \rho C_V \Delta T dV = \frac{1}{\gamma - 1} \Delta P V \quad (2)$$

where ΔT and ΔP are the temperature and pressure increase in the test volume. Heating capacities C_V , heat capacity ratio γ and the chamber volume V are assumed to be constant.

The closed volume is a cylindrical chamber. It is made of POM-C, to reduce heat losses through the walls, and there are 25 mm diameter silica windows with anti-reflection coated surfaces (W2-PW1-2506M-UV-1064-0) at the cylinder bases. This chamber ensemble is shown in Fig. 8. The resulting volume of the chamber is $V = 19.6 \pm 0.2$ ml and it was chosen in order to facilitate the pressure rise measurement. The volume was verified by filling it with water with a volumetric syringe. Because the transient increase pressure produced by an electrical discharge of few hundred mJ is of a few mbar in such a volume, a piezoresistive differential pressure transducer Meggitt 8510B-1 (0-1 psi range) is used. It is connected to a Meggitt DC Amplifier model 136, which also adapts and filters the pressure signal, with an integrated 10 kHz Butterworth physical filter (cf. red curve in Fig. 10). Signals are recorded by a LeCroy waverunner 104Xi high speed sampling oscilloscope. The transducer is located at least 1 cm from the electrodes tips and is protected by a porous metallic disc (around 50% porosity) to reduce the direct impact from the shockwave at breakdown. In this chamber, the maximum uncertainty is estimated at 6% for a discharge at $E_{th} = 100$ mJ. A pressurized system (a parallelepipedal counter pressure chamber) is used for experiments involving different gas pressures. It consists of an outer metallic chamber which contains the calorimetry chamber test (see Fig. 8). The counter pressure chamber is made of stainless steel, measuring 120x76x70 mm³, with a 0.64 dm³ inner volume. It serves as a reference pressure for the piezo-resistive differential pressure transducer. Such configuration allows keeping a good accuracy on the pressure measurement in the calorimetry chamber test. A gas inlet at the base, closed by a valve, allows filling and emptying the volume with gas at different pressures. Two opposite sides of the chamber hold 125x75 mm² windows for visualization diagnostics.

In order to remove the resonance frequency of the chamber, the recorded pressure signal is processed by suppressing frequencies over 4 kHz in the Fourier domain before performing the inverse transform (blue curve in Fig. 9). The thermal energy released to the gas is then obtained from the filtered unsteady pressure evolution a few milliseconds after the discharge, averaged over 1 ms (green curve in Fig. 9). A set of 45 tests, performed at ambient pressure in air, indicates that the electrical to thermal efficiency of this igniter is on average 13.7%, with an average electrical energy used of 625 mJ (see Fig.

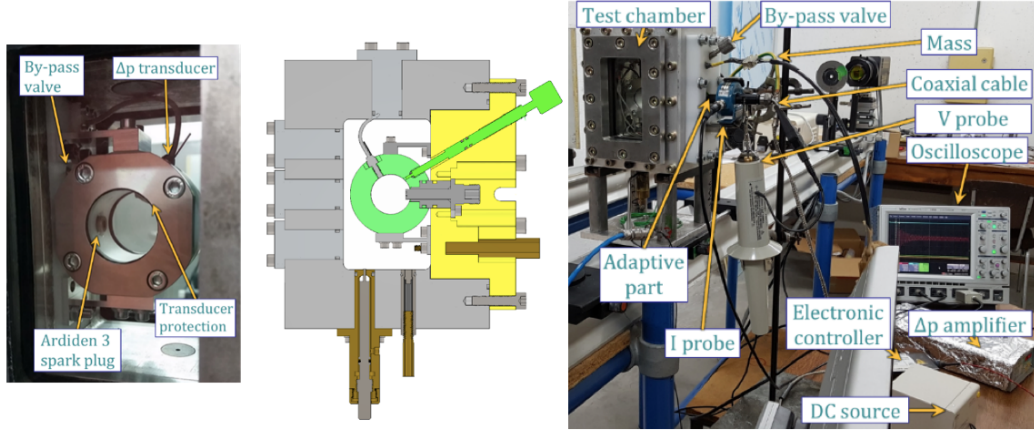


Figure 8: Calorimetry setup: detail of the 20 ml cylinder (left) and sketch and overview of the full calorimetry setup with the counter pressure chamber (center and right): 20 ml inner volume chamber (light green), by-pass valve (green), pressure transducer and spark plug (grey) and POM-C wall (yellow).

10). The corresponding standard deviations are 49 mJ, 7 mJ and 0.4% for the electrical energy, thermal energy and efficiency respectively. This scattering results from the stochastic nature of the ignition process. Among the different causes, one may evoke microscopic differences in the surface of the electrodes between consecutive discharges and the scattering in the formation process of the plasma channel. Tests performed at different pressures have shown a very weak influence of gas pressure on the global features of the discharges of this igniter. The efficiency ranges from 12 to 14% when increasing gas pressure from 0.25 to 2 bar (in particular: 12.5% for 0.5 bar and 13.7% for 1 bar).

2.3. Ignition Kernel Spatial Characteristics

To determine the kernel size evolution and its projection from the igniter, high magnification Speckle Background Oriented Schlieren (SBOS) visualization developed in a previous study [24] has been used. Such technique highlights the density gradient, which is related to the refraction index gradient through the Gladstone-Dale relation.

The light source is a diode-pumped continuous solid-state laser (MxL-F, $\lambda = 532$ nm, 3 W). The emission power is stabilized for steady conditions at 1%. The beam is expanded to a 45 mm diameter parallel beam by a collimator impacting a 1 mm wide ground glass that produces the speckle by

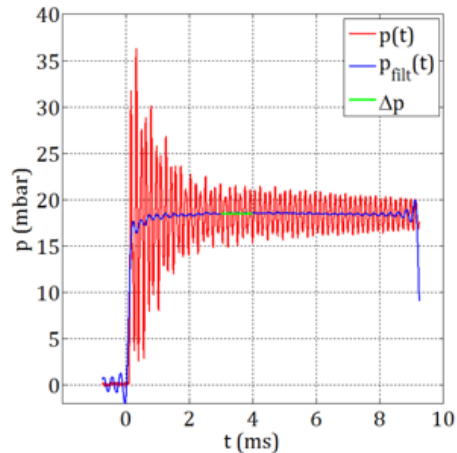


Figure 9: Typical time-pressure evolution measured and filtered in the micro-calometric chamber (right).

scattering effects. In order to record sufficiently sharp images of the kernel and of the generated shock wave, the exposure time is reduced down to $1 \mu\text{s}$ using a Princeton CCD intensified camera (PiMax 1k GenII RB-SG). A 532 nm interferometric filter is used to reduce the light emission from the hot kernel. The deviations of light rays due to refractive index variations induce displacements of the speckle patterns that are determined by PIV-like multipass cross correlation processing [24]. Time evolution of the kernel is then reconstructed by test repetition, shifting the delay between the spark trigger and the image timing. The resulting displacement fields are reported in Fig. 11 for ambient pressure showing the expansion of the kernel with time as well as the shock wave propagation.

The kernel penetrations, defined as the distance between igniter surface and tip of the kernel and the kernel volume obtained from a cylindrical symmetry assumption, are determined from these visualizations for two pressure values, as reported in Table 1 at a given delay after the spark.

Table 1: Geometrical characteristics of the hot kernel obtained from Schlieren images

Pressure (bar)	Kernel thermal E. (mJ)	Penetration (mm)	Kernel Vol. (mm^3)	Delay (μs)
0.5	72	6.2	≈ 330	57
1	85	5.3	≈ 280	48

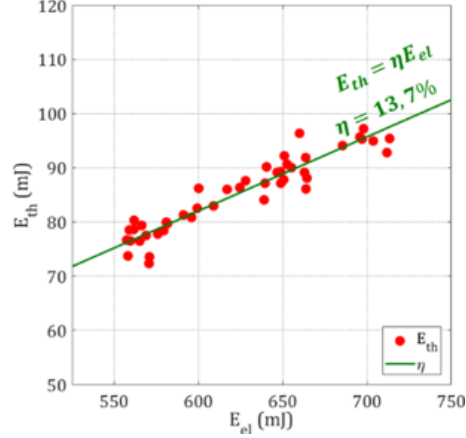


Figure 10: Electrical (E_{el} , abscissa) to thermal (E_{th} , ordinates) energy correlation for the Ardiden 3 igniter at ambient pressure

3. Numerical modelling

The three-dimensional compressible LES code AVBP from CERFACS (www.cerfacs.fr/avbp7x) has been used. It solves the LES filtered compressible Navier-Stokes equations (mass, momentum, energy and $N_s - 1$ species) which read:

$$\frac{\partial \bar{\rho}}{\partial t} + \frac{\partial (\bar{\rho} \tilde{u}_i)}{\partial x_i} = 0 \quad (3)$$

$$\frac{\partial \bar{\rho} \tilde{u}_i}{\partial t} + \frac{\partial (\bar{\rho} \tilde{u}_i \tilde{u}_j)}{\partial x_j} = - \frac{\partial (\bar{P} \delta_{ij} - \bar{\tau}_{ij} - \bar{\tau}_{ij}^t)}{\partial x_j} \quad (4)$$

$$\frac{\partial \bar{\rho} \tilde{E}}{\partial t} + \frac{\partial (\bar{\rho} \tilde{E} \tilde{u}_j)}{\partial x_j} = - \frac{\partial [u_i (\bar{P} \delta_{ij} - \tau_{ij}) + \bar{q}_j + \bar{q}_j^t]}{\partial x_j} + \bar{\omega}_T + \bar{Q} \quad (5)$$

$$\frac{\partial \bar{\rho} \tilde{Y}_k}{\partial t} + \frac{\partial (\bar{\rho} \tilde{Y}_k \tilde{u}_j)}{\partial x_j} = - \frac{\partial [\bar{J}_{j,k} + \bar{J}_{j,k}^t]}{\partial x_j} + \bar{\omega}_k \quad (6)$$

where the overline indicates the filtered elements and tilde the Favre-filtered terms. $\dot{\omega}_k$ stands for the chemical source terms, while $\dot{\omega}_T$ accounts for the energy change due to chemical reactions, \dot{Q} indicates energy sources such as the one provided by the ignition system. The perfect gas law is used.

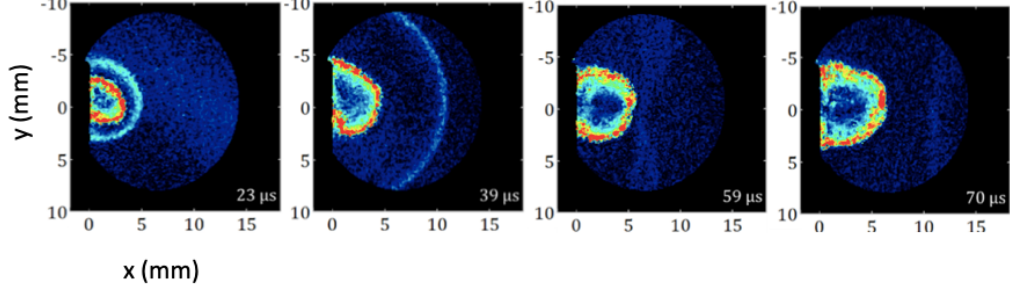


Figure 11: Ardiden 3 igniter discharge kernel evolution for P=1 bar and T=293 K. Visualisation for 23, 39, 59 and 70 μs after start of the spark. Positions are reported in mm from the igniter surface, along the symmetry axis.

The filtered viscous flux, heat flux and species diffusion terms are modelled as:

$$\bar{\tau}_{ij} \approx \bar{\mu} \left(\frac{\partial \tilde{u}_j}{\partial x_i} + \frac{\partial \tilde{u}_i}{\partial x_j} - \frac{2}{3} \delta_{ij} \frac{\partial \tilde{u}_k}{\partial x_k} \right) \quad (7)$$

$$\bar{q}_i \approx \bar{\lambda} \left(\frac{\partial \bar{T}}{\partial x_i} + \sum_{k=1}^N \overline{J_{i,k} \tilde{h}_{s,k}} \right) \quad (8)$$

$$\overline{J_{i,k}} \approx -\bar{\rho} \left(\bar{D}_k \frac{W_k}{W} \frac{\partial \tilde{X}_k}{\partial x_i} - \tilde{Y}_k \tilde{V}_i^c \right) \quad (9)$$

where $h_{s,k}$ is the sensible enthalpy for species "k", D_k is the mass diffusivity of species "k", W and W_k the molecular weight of the mixture and species "k" respectively, and v^c stands for the correction velocity used to ensure mass conservation, which follows the Hirschfelder formulation [25]. More details about the modelling of each term can be found in [26]. The respective subgrid components are denoted by the "t" superscript in Eqs. 7 to 9. For the momentum equation, the SIGMA turbulent subgrid model [27] is used. The interaction of the flame with turbulence is modelled using the thickened flame model. In this study, the flame sensor recently proposed in [28] is used which automatically identifies the heat release zones and applies thickening according to a single user-specified number of cells within the flame front (in this study 7 cells). This sensor has the advantage of being independent of flow conditions (equivalence ratio, pressure, etc.) and to adapt automatically to the mesh resolution. In order to describe the non-resolved flame wrinkling

due to subgrid-scale turbulence, the thickened flame model [29] uses the efficiency function Ξ_Δ , also known as wrinkling factor. In this work, both the static and the dynamic formulations of the efficiency developed in [30] are tested and compared.

The wrinkling factor is defined as:

$$\Xi_\Delta = \frac{S_{T\Delta}}{S_L^0} = \frac{A_{sgs}}{\Delta^2} \quad (10)$$

where Δ is the length scale associated to the LES filtering, $S_{T\Delta}$ is the turbulent flame speed at the subgrid scale level, S_L^0 is the laminar unstretched flame speed and A_{sgs} the subgrid scale flame surface area. Both static and dynamic formulations assume equilibrium between the turbulent motion and the flame wrinkling. This assumption is valid as long as the time scales associated to subgrid-scale flame dynamics are much smaller than the other time scales of the flow field [30].

The static formulation postulates the following expression for efficiency:

$$\Xi_\Delta = \left(1 + \min \left[\left(\frac{\Delta}{\delta_l^0} - 1 \right), \Gamma_\Delta \left(\frac{\Delta}{\delta_l^0}, \frac{u'_\Delta}{S_L^0}, Re_\Delta \right) \frac{u'_\Delta}{S_L^0} \right] \right)^\beta \quad (11)$$

where Re_Δ and u'_Δ are the Reynolds number at subgrid-scale and the corresponding velocity fluctuation, δ_l^0 is the laminar unstretched flame thickness and Γ_Δ is a function that accounts for the straining effects of the vortices smaller than Δ on the flame, obtained in [30] from DNS calculations. In this study, like in [31], the velocity fluctuation is calculated from the rotational part of the resolved velocity field. In the static formulation, a constant value of $\beta = 0.5$ is used as suggested in [30]. The dynamic formulation introduces a non-constant β coefficient, which is dynamically computed [32, 33]. The dynamic computation is performed with a double filtering operation, equating the flame surfaces calculated at a filtered and test-filtered scales and employing a ‘‘Germano-like’’ equation shown in Eq. (12).

$$\left\langle \overline{\Xi_\Delta \frac{W_\Delta(\hat{q})}{\Delta}} \right\rangle = \left\langle \Xi_{\gamma\Delta} \frac{W_{\gamma\Delta}(\hat{\hat{q}})}{\gamma\Delta} \right\rangle \quad (12)$$

where γ is the ratio of a test filter scale to Δ , the test filter at scale $\gamma\Delta$ is denoted by a top hat and the right and left brackets denote spatial averaging.

W_{Δ} is the resolved reaction rate, expressed as function of a temperature based progress variable q . In this study, γ is set to 1.5. Previous works [31, 32] suggest that this parameter does not have a strong impact on the simulations when $1.5 < \gamma < 7$. Applying Eq. (10) to express the wrinkling factors gives an equation for β . In this work, the local formulation is used, in which the previously mentioned equality is enforced over a control volume denoted by $\langle \cdot \rangle$. Further details of how the β parameter is calculated can be found in [33].

The second-order explicit Lax-Wendroff scheme was used with a time step constrained by both the CFL condition and chemical activity and was of order $O(10ns)$.

Three different tetrahedral meshes were used during this study. During the filling phase of each case, a coarse 18-million cell mesh was used with a mesh size of 0.2 mm in the injection channel and 0.33 mm for the rest of the chamber. During the ignition phase, this coarse mesh is refined in a spherical region around the igniter of 10 mm of radius with a resolution varying linearly between $75 \mu\text{m}$ and 0.33 mm at the external radius in order to resolve the strong temperature gradients. Most importantly, this refinement avoids the use of the thickened flame model during the first instants of ignition when the kernel does not have a propagating flame structure [34]. One millisecond after energy deposition finishes, the third and final mesh is used with a uniform cell size of 0.2 mm everywhere (44 million cells). Note that y^+ remains below 30 in all the wall regions.

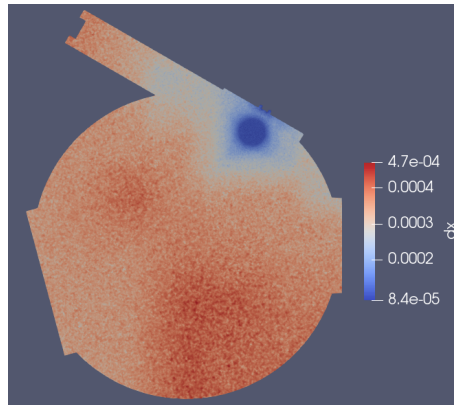


Figure 12: Overview of the mesh with mesh sizes in m used during the energy deposition instants showing mesh refinement near the igniter

3.1. Initial and Boundary conditions

For the laminar cases, all surfaces were treated as non-adiabatic walls, using heat transfer resistances obtained with the electric analogy and equal to $1.43\text{e-}2 \text{ m}^2\text{K}/\text{W}$ for the quartz boundaries (the cylinder faces) and $2.18\text{e-}2 \text{ m}^2\text{K}/\text{W}$ for the steel boundaries (rest of boundaries) and assuming the surrounding air at ambient conditions. The laminar cases were initialized with a quiescent premixed mixture of methane and air at the corresponding conditions.

For the turbulent cases, in the experiments, the filling of the chamber starting from vacuum to 1 bar lasts 135 ms (67.5 ms for 0.5 bar). This procedure was reproduced numerically. Due to the pressure ratio between the tank (6 bar) and the chamber ($0 < p < 1$ bar), the injector nozzle is choked throughout the filling process. Following the measured linear increase in pressure with time during filling, a constant uniform mass flow rate boundary at a constant temperature of 387 K was imposed at the inlet. This approach does not take into account the true shape of the inlet velocity profile, but the lack of measurements at the inlet did not allow to do better. The solid walls are treated with wall-functions. Both pressure and density at the end of injection were verified to be within 1% of the experiment, which gives confidence to the numerical setup during the filling phase. Once the desired pressure is reached, injection stops and the inlet boundary is modelled as a wall.

3.2. Chemical scheme

The analytically reduced chemistry for methane/air employed is described in [35] and consists of 19 species and 184 reactions (Lu19). This scheme has been thoroughly validated for auto-ignition (for $1000 < T < 8000$ K), 1D flames, perfectly stirred reactors for $1 < p < 30$ atm and has been recently used in the ignition study in [36]. Within the context of this study, this scheme has been compared to the skeletal mechanism GRI 3.0 and an in-house 22 species methane scheme (S22R195, derived from the detailed scheme from the CRECK group at PoliMi [37]) in a counterflow premixed flame at different operating conditions as detailed in [38]. Results show a maximum difference of 15% in consumption speed and 10% in species profiles for strain levels ranging from 0 to 20000 s^{-1} . A summary of these results for inlet conditions of $p=1$ bar, 320K and $\phi = 0.83$ is shown in Fig. 13 and Fig. 14. These conditions are representative of operating conditions under study.

Note that the species H_2O_2 and HO_2 had to be implicated following the methodology described in [26] to avoid numerical oscillations.

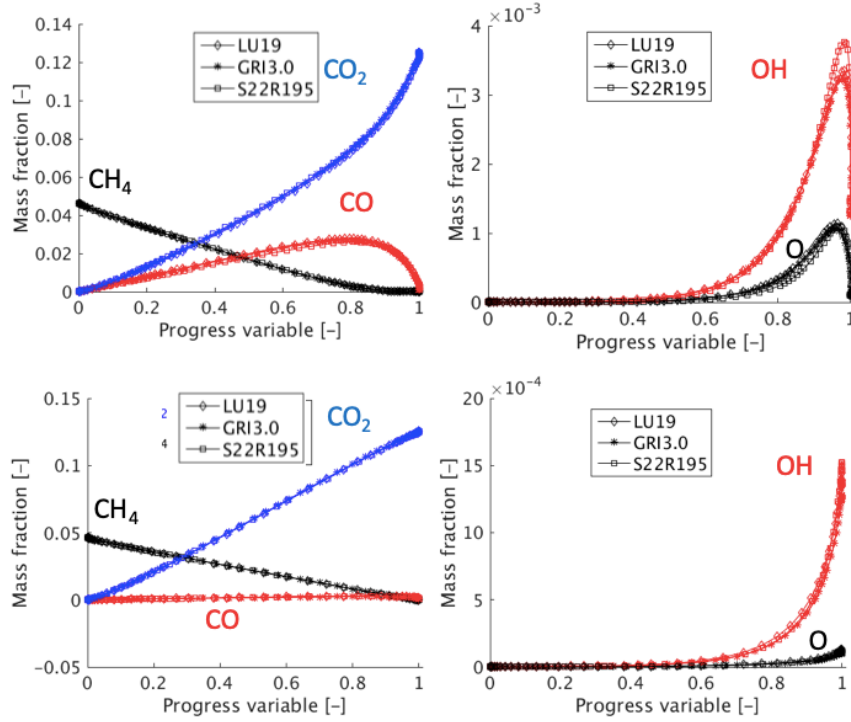


Figure 13: Methane-air combustion: comparison of species profiles in a lean premixed flame for inlet conditions of $p=1$ bar, 320K and $\phi = 0.83$ at strain rate equal to 2000 s^{-1} (top) and 20000 s^{-1} (bottom) or Lu19, GRI3.0 and S22R195. Progress variable based on CH_4 .

3.3. Ignition modelling

The energy supplied by the igniter was modelled as a source term in the energy equation following the model in [39]. The temporal evolution of power of this igniter measured in the experiment was introduced in the model. This power profile was shown in Fig. 7 (right). Note that the amount of energy is higher and the deposition time lower than in conventional ignition systems such as pin-pin electrodes [5]. Two electrical to thermal efficiency values were used during the energy deposition. For the breakdown ($t < 20\text{ns}$), $\eta = 0.95$, similarly to [5], while the rest of the process used a constant efficiency measured in the experiment equal to 0.137. To avoid any bias due

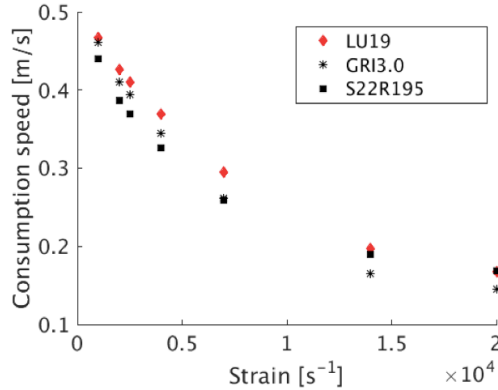


Figure 14: Consumption speed versus strain rate for a strained premixed flame at inlet conditions of $p=1$ bar, 320 K and $\phi = 0.83$ for Lu19, GRI3.0 and S22R195

to the igniter model parameters, the volume where energy is deposited is a sphere whose radius and position have been adjusted so as to match the kernel penetration depth observed at several pressure conditions and times (as in Table 1). The deposited energy spatial profile has a hyperbolic tangent shape so as to provide a smooth transition to zero outside the ignition zone. The maximum temperature attained at the kernel location is approximately 10000 K. All thermodynamic properties were obtained from the reference NASA database [40] up to 5000 K and extrapolated to higher values assuming constant C_p and γ equal to those at $T=5000$ K.

4. Results

4.1. Laminar case

In order to validate the modelling of the wall heat losses, a laminar case with $p_{ini} = 1bar$, $T_{ini} = 300K$ and $\phi = 0.7$ was performed. Fig. 15 shows the Schlieren and density gradient images at $t=38$ ms and Fig. 16 shows the temporal evolution of pressure up to 45 ms. The same propagation speed was recovered as in the experiments. This offers evidence that heat losses are well modelled for this configuration.

4.2. Turbulent cases: non-reacting filling phase

Three operating conditions are discussed in detail and are presented in Table 2 and are representative of the operating conditions of an actual Safran

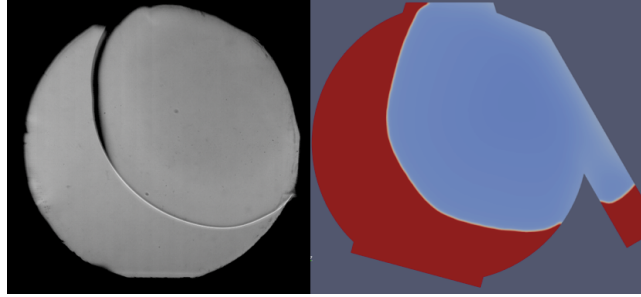


Figure 15: Flame visualization at $t=38$ ms after sparking. Experiment Schlieren (Left). Computation: normalized density field (Right)

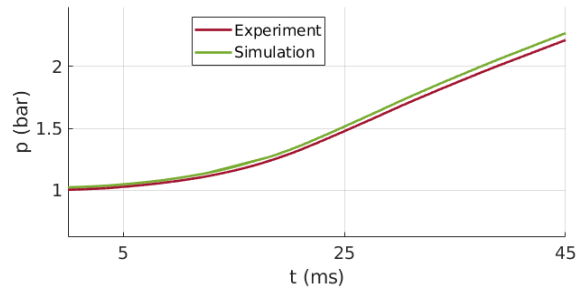


Figure 16: Temporal pressure evolution for a case with $p_{ini}=1\text{bar}$, $T_{ini}=300\text{ K}$, $\phi=0.7$

SCT engine. All were performed with a $\phi = 0.7$ mixture. Turbulent case A is characterized by injection at 1 bar (lowest injection velocity, note that inlet is a constant mass flow rate boundary, thus velocity diminishes as the density increases as the chamber fills up), and a short delay between end of injection and sparking (5ms), which results in high turbulence intensity and, therefore, a high Karlovitz number (Ka). Turbulent case B ignition starts at 0.5 bar (highest injection velocity) and has the same delay of 5 ms, thus also having a strong turbulent intensity. However, Ka has changed due to faster diffusion. Finally, turbulent case C also starts at 0.5 bar (higher injection velocity), but its longer delay (30 ms) attenuates the turbulence intensity with respect to cases A and B. The three cases also feature different strain rate at the igniter location, highest for case B.

The turbulent field is well resolved except for small regions where recirculation occurs (injector exit and corners), as can be seen in Fig. 17 and Fig. 18 showing fields of ν_{turb}/ν_{lam} . Fig. 20 shows the probability density function (PDF) of tangential and radial velocities around the igniter observed in

Table 2: Cases under study. Ignition delay refers to the time between the end of injection and sparking. The turbulence and strain levels are obtained from the tangential velocity at a position 1 mm above the igniter and are averaged values over ± 1 ms around the time of sparking

Case name	P at end of injection	Ignition Delay	Strain level at igniter start	Ka	Re
Case A	1 bar	5 ms	3600 s^{-1}	63.2	31200
Case B	0.5 bar	5 ms	5500 s^{-1}	3.4	22200
Case C	0.5 bar	30 ms	3300 s^{-1}	0.6	13900

cases at the sparking instant for cases A, B and C. The wider distributions in A and B (short delays) with respect to C (long delay) give evidence of higher turbulence levels. On the other hand, the mean value of the tangential velocity in B corroborates the higher injection velocity compared to cases A and C.

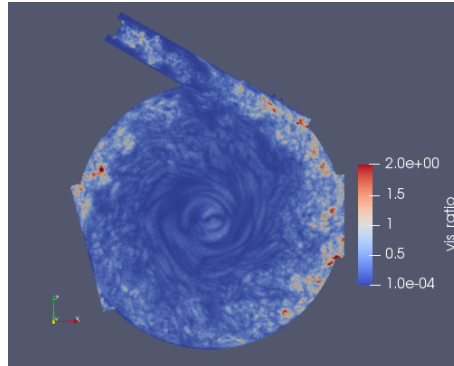


Figure 17: Field of ν_{turb}/ν_{lam} after filling up to $p=1$ bar for case A, before spark

4.3. Turbulent cases: reacting phase using the static efficiency formulation

Figure 19 shows a comparison of the temporal evolution of pressure between experiments and LES for the three cases. The time for maximum pressure in case A is smaller than cases B and C due to the higher Ka (more flame surface wrinkling). This is manifested by a higher efficiency value for case A, as it will be shown later in this section. A comparison of Schlieren images from experiments and LES density-gradient line-of-sight integration (LOS) can be found in the Supplementary Material. The pressure curve

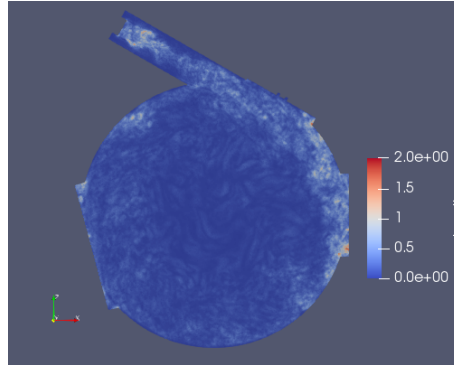


Figure 18: Field of ν_{turb}/ν_{lam} after filling up to $p=0.5$ bar for case B, before spark

and image series demonstrate an overall good agreement between LES and experiments for all cases. Although the temporal evolution of pressure curves of cases A, B and C are different, they can be decomposed into similar phases, which will be explained.

In case A, both experiment and LES show a small pressure rise during the first 5 ms after spark (phase a), where the flame kernel propagation is governed mainly by the flow straining effects and is only weakly affected by turbulence. After the kernel has reached the chamber center at $t \approx 5$ ms, it starts to expand radially (phase b). During this phase, pressure increases fast and at an approximately constant rate. This behavior is also shown graphically in the LOS images in the Supplementary Material. LES displays a slightly delayed kernel rotation. This effect may be attributed to the uniform mass flow rate boundary which does not take into account the actual shape of the inlet velocity profile. Around $t \approx 10$ ms, a slight change of slope in the LES indicates the acceleration of the burning rate (phase c). Complete combustion is reached at $t \approx 20$ ms.

In case B, identically to case A, both the experiment and LES show a weak pressure rise while the flame kernel is being strained and travels towards the center of the chamber (phase a). It is followed by a radial expansion (phase b), where the flame kernel expands radially at a constant rate. This behavior is well represented in LES. After $t \approx 20$ ms, the third phase (phase c) is much more visible. As for case A, in this phase, the consumption speed in LES is faster than in experiments. This reaction acceleration when the flame comes closer to the walls is linked to the interaction of the flame with the vorticity generated near the walls.

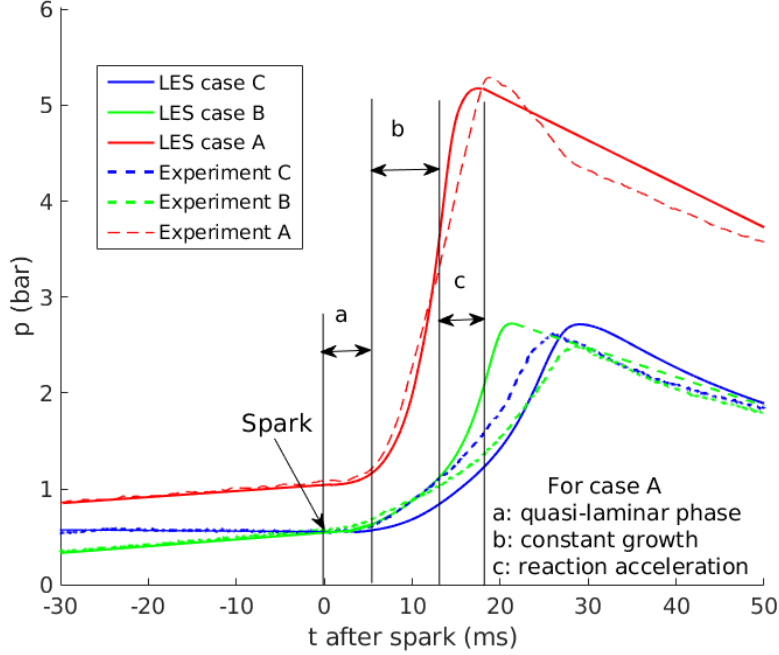


Figure 19: Temporal evolution of pressure for cases A, B and C. The evolution in all cases can be divided in three phases: a) weak turbulence interaction b) constant flame growth c) burning rate acceleration

Case C has an overall similar behavior to cases A and B, but the pressure rise is delayed to $t \approx 10$ ms. Phase b is delayed until $t \approx 20$ ms, and acceleration occurs then to reach complete combustion at $t \approx 30$ ms in the LES and 25 ms in the experiments. The pressure rises when the flame comes closer to the walls, which results in a narrowing of the delay between LES and the experiment. Similarly to cases A and B, this behavior can also be seen in the LOS images in the Supplementary Material.

In summary, the overall agreement is fairly good, and the pressure rise and kernel shape are well modelled with small time differences. In case A, the LES calculation predicts the pressure peak at $t = 17$ ms, 2 ms before the experiment. In case B, the anticipation is greater and the LES and the experiment reach the pressure peak at $t = 21$ ms and 28 ms respectively. Finally, in case C, the time to reach the pressure peak in the calculation is 29 ms, which is 1 ms longer than in the experiment. To better understand the

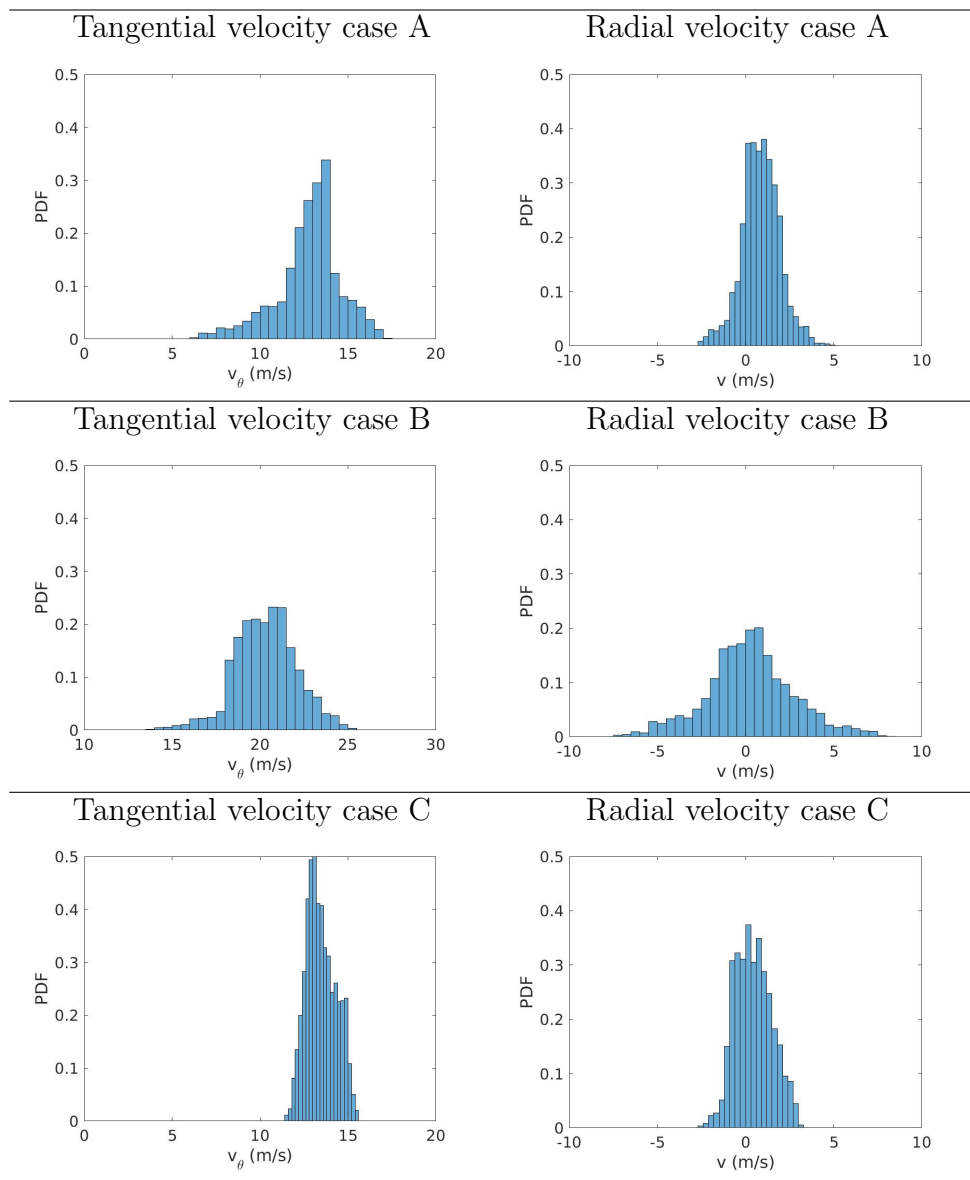


Figure 20: Comparison of PDFs of tangential and radial velocities in a sphere of $R=3.5\text{cm}$ around the igniter location at the time of spark for the three cases

turbulent flame behavior, additional analysis of the LES is now performed.

Fig. 21 shows the numerical temporal evolution of the resolved surface-to-volume ratio of the flame kernel S/V using an isovolume of progress vari-

able based on temperature at the value $q = 0.65 \pm 0.15$. For all cases, S/V grows with time as the flame becomes more wrinkled due to turbulence. Note that the evolution of S/V shows a linear growth in time that does not replicate the pressure rise acceleration when the flame approaches the walls ($t \approx 10ms$ for cases A and B). This indicates that the pressure rise, proportional to the total heat release rate, is not only sensitive to the increase of flame surface area due to resolved flame wrinkling, but also to the local burning intensity.

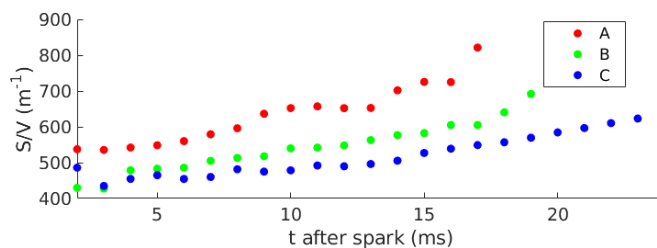


Figure 21: Temporal evolution from LES of the surface to volume ratio of the kernel S/V for the three cases

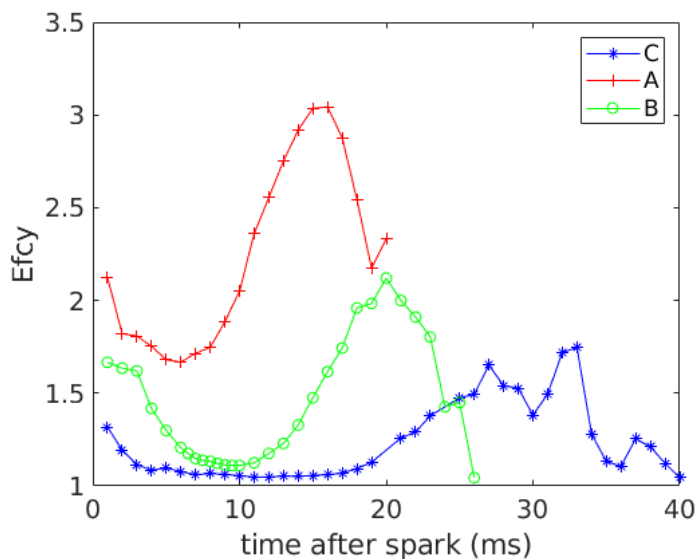


Figure 22: Temporal evolution of the average value of efficiency in $q = 0.65 \pm 0.15$ for the three cases

To further investigate this question, Fig. 22 shows the temporal behavior of the efficiency function averaged over the region $q = 0.65 \pm 0.15$ for the three cases. Higher efficiency values are accompanied by higher consumption speeds. The evolution of the three cases is very similar to the pressure curves in Fig. 19. For $t < 5ms$ (phase a) efficiency decreases and reaches a minimum. Efficiency starts to grow again when the flame stabilizes around the center of the chamber (phase b). Finally, there is a noticeable increase of efficiency when the flame comes closer to the walls (phase c) (case A; $t \approx 10ms$, and case B; $t \approx 20ms$).

The impact of the walls is confirmed in Fig. 23, showing only the regions where wall-originated vorticity interacts with the flame have an efficiency increasing noticeably over 1.

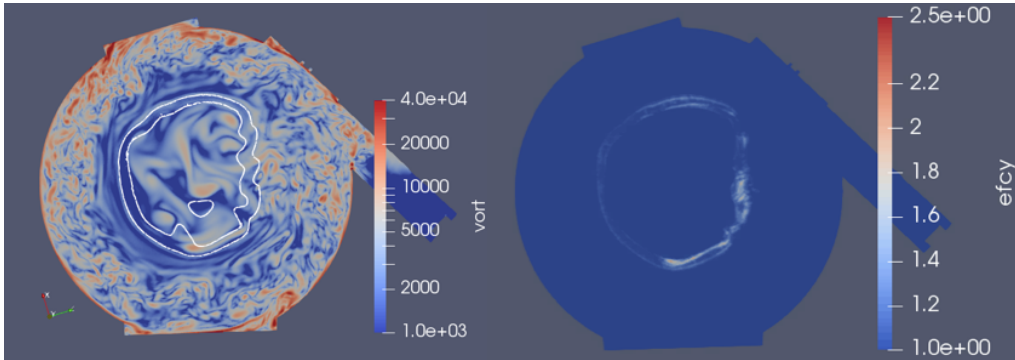


Figure 23: Left: Vorticity field with a white contour indicating flame position for case B at $t=6ms$ after spark. Right: Efficiency field showing high values only where wall-originated vorticity is interacting with the flame.

Because the interaction between the turbulence at the walls and the flame as well as the compression caused by the flame expansion may not be well modelled with the static formulation of efficiency, the dynamic formulation of efficiency is now studied.

4.4. Turbulent cases: using the dynamic efficiency formulation

In the static efficiency formulation, the coefficient β is a constant set to 0.5 based on standard academic turbulent flows. It has been however demonstrated that β may vary significantly in transient cases or complex turbulent flows. As the discrepancies between LES and experiment are here attributed to the incorrect efficiency function near the walls when β is fixed to

0.5, a more accurate formulation is attempted with the dynamic formulation presented in Section 3.

Figure 24 shows the pressure evolution obtained with both formulations of efficiency. From spark to the constant radial growth phase (phases a and b), both static and dynamic efficiency formulations predict the same rate of pressure increase. As expected, the difference becomes visible when the flame approaches the walls, where the dynamic modelling predicts a lower consumption speed, hence slower pressure rise, than the static model for all cases: case A attains its peak at $t=19$ ms (+2 ms compared to the static efficiency formulation), case B at $t=27$ ms (+6 ms compared to the static formulation) and C at $t=31$ ms (+2 ms compared to the static formulation). To be compared to the experimental peaks reached at $t=19$, 25 and 28 ms respectively. Interestingly in [31], a study of ignition in the MICCA-spray setup, found a 15% to 20% reduction in the consumption speed when employing the dynamic efficiency function with respect to the static version. This reduction, which was determined to be linked to a reduction in the subgrid-scale wrinkling, caused a corresponding increase in ignition delay time of the same magnitude as in the present study.

The figures in Fig. 25 clearly indicate that the lower consumption speed predicted with the dynamic formulation is directly linked to lower values of efficiency at times $t > 7$ ms.

Figure 26 reveals that for these conditions, on average, the parameter β is smaller than the fixed value assumed in the static formulation $\beta = 0.5$. In particular, β only nears 0.5 in isolated highly curved regions.

Figure 27 displays the temporal evolution of the volume-averaged value of β over the isovolume of $q = 0.65 \pm 0.15$. For all cases, the average β increases from the start to the point of maximum pressure. During the first instants, the kernel develops far from the walls and the effect of turbulence on the kernel is weak. As the kernel expands radially, it interacts with the vorticity generated at the walls and this is translated into higher values of β . The case initially at atmospheric pressure (case A) shows the highest increase, starting at an average value of β equal to 0.2 and increasing to 0.5. For cases B and C, the averaged value of β starts at 0.1 and increases to 0.2 approximately. Results in Fig. 27 are consistent with the high Karlovitz number in case A. The average efficiency value being closer to 0.5 is also consistent with the moderate impact of the dynamic efficiency for case A.

Probability density functions of β for cases A, B, C for an isosurface of $q = 0.5$ are shown in the Supplementary Material. They all show a mostly

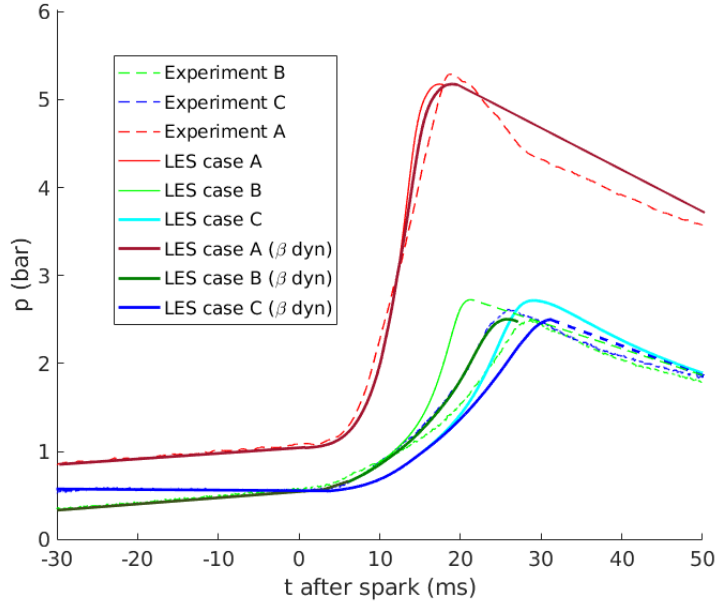


Figure 24: Left: Pressure time evolution for the three cases obtained with the static and the dynamic efficiency formulations and compared to experiments

monomodal distribution with an average of 0.15 (cases B and C) and 0.35 (case A). As a comparison in [31], the ignition of the annular MICCA-spray chamber led to bimodal β distributions, the first peak centered around 0.15 and the second peak at 0.65 (the second peak associated to the flame region near the injectors). In the present configuration, the flame is subjected to comparable levels of wrinkling corresponding to the low values of β . Because there is no flame-anchoring mechanism, no high values of β are found. The PDF of β becomes narrower with time indicating the transition between an isothermal turbulent flow field to a growing hot gas expansion flow.

4.5. Impact on computational cost

Each calculation with the static version of efficiency necessitated on average 483,000 processor hours to be completed. On the other hand, the use of the dynamic formulation required an average of 1,161,000 processor hours due to the additional filtering operations to calculate the parameter β . However, studies such as [31] have reduced this additional cost by introducing a modification in which the additional operations for the dynamic formulation

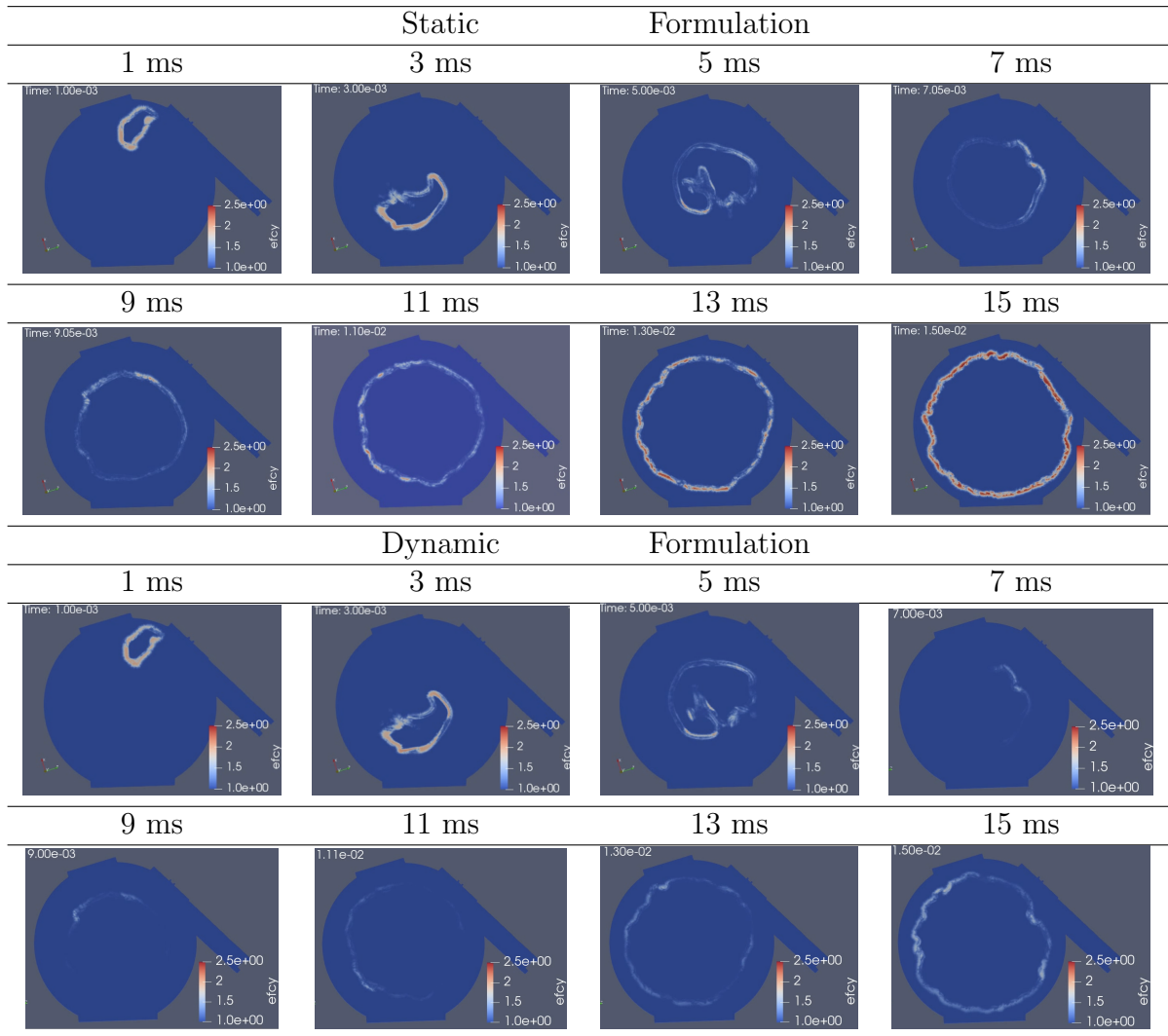


Figure 25: Comparison of static and dynamic efficiency values in the middle plane for case B showing lower efficiency values of the dynamic formulation at later instants. Top: static formulation, bottom: dynamic formulation. Time after spark

are only performed in the regions of the domain where thickness is greater than one. As a result of that, [31] reported an increase of 15% when using the dynamic efficiency with respect to the static formulation, while ensuring that the PDF β remained identical to the case where the filtering operations were applied to the whole domain.

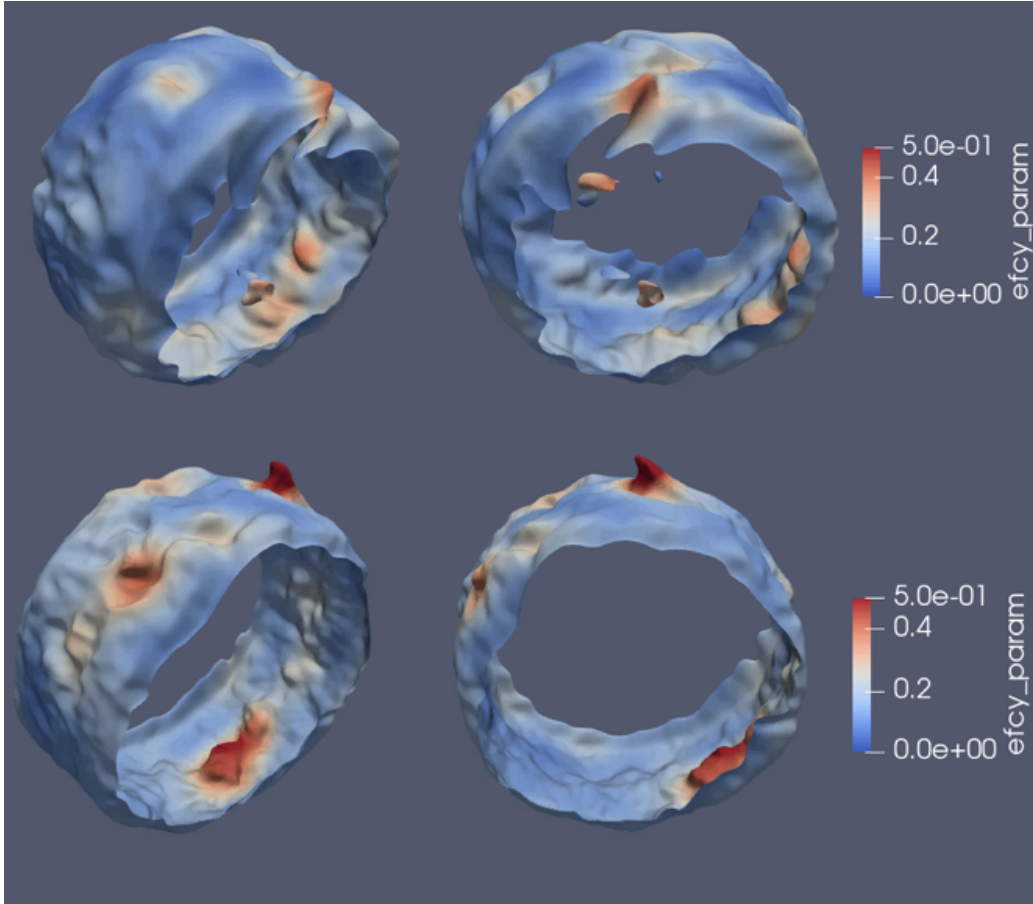


Figure 26: Case B lateral and frontal views of β for an isosurface of $q=0.5$ at $t=15$ ms (up) and $t=20$ ms after spark (bottom) showing that, on average, $\beta < 0.5$ for these conditions

5. Conclusions

Ignition in a lab-scale configuration reproducing conditions of a SCT chamber has been studied both experimentally and numerically by means of LES. It was found that the numerical methodology allows the reproduction of the first instants of ignition including flame kernel formation and initial propagation with overall good agreement at several conditions relevant to aero-engine operation.

The dynamic formulation of the efficiency function is able to reproduce all the phases of the process, and the maximum error in the time to reach pressure peak is 10% across all conditions. On the other hand, the maximum

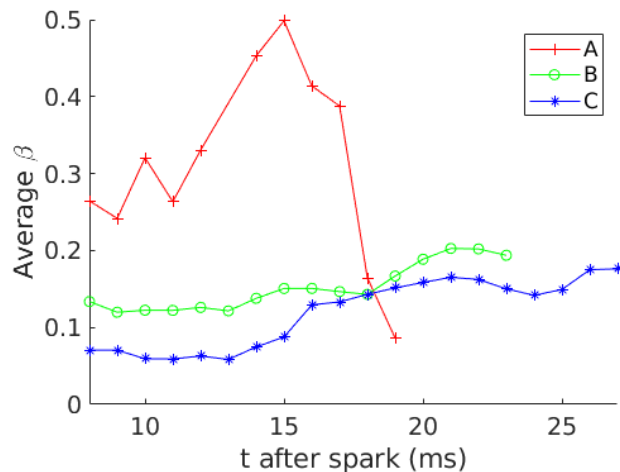


Figure 27: Evolution of the volume integral of the wrinkling parameter β over an isovolume of $q = 0.65 \pm 0.15$

error in the static formulation is 20%. The main difference between formulations is the smaller value of efficiency in the dynamic case when the flame interacts with vorticity generated at the walls. This is due to the fact that the efficiency parameter (β) is generally not equal to the value in the static formulation (0.5).

Acknowledgements

This work is part of EU Commission project Annulight (European Union’s Horizon 2020 research and innovation programme under Grant Agreement No 765998). HPC resources from the TGCC Grands Challenges Project N°gch0513 (SPIN360) are also acknowledged.

References

- [1] N. Savary, G. Taliercio, The Safran helicopter engine spinning flame combustor concept to meet customer needs, 42nd European Rotorcraft Forum, Lille, France, 2016.
- [2] E. Mastorakos, Forced ignition of turbulent spray flames, Proc. Combust. Inst. 36 (2017) 2367–2383.

- [3] F. Collin-Bastiani, Modeling and large eddy simulation of two-phase ignition in gas turbines, Ph.D. thesis, Institut National Polytechnique de Toulouse (2019).
- [4] T. Lancien, Etude numérique de l'allumage diphasique de foyers annulaires multi-brûleurs, Ph.D. thesis, Université Paris-Saclay (2018).
- [5] F. Collin-Bastiani, et al., DNS of spark ignition using Analytically Reduced Chemistry including plasma kinetics, *Proc. Combust. Inst.* 37 (2019) 5057–5064.
- [6] B. Sforzo, A. Lambert, J. Kim, J. Jagoda, S. Menon, J. Seitzman, Post discharge evolution of a spark igniter kernel, *Combust. Flame* 162 (2015) 181–190.
- [7] D. R. Ballal, A. H. Lefebvre, The influence of flow parameters on minimum ignition energy and quenching distance, *Symp. (Int.) Combust.* 15 (1974) 1473–1481.
- [8] A. D. Birch, D. R. Brown, M. G. Dodson, Ignition probabilities in turbulent mixing flows, *Symp. (Int.) Combust.* 18 (1981) 1775–1780.
- [9] S. Ahmed, E. Mastorakos, Spark ignition of lifted turbulent jet flames, *Combust. Flame* 146 (2006) 215–231.
- [10] H. K. Reddy, J. Abraham, Influence of turbulence–kernel interactions on flame development in lean methane/air mixtures under natural gas-fueled engine conditions, *Fuel* 103 (2013) 1090–1105.
- [11] L. Esclapez, Numerical study of ignition and inter-sector flame propagation in gas turbines, Ph.D. thesis, Institut National Polytechnique de Toulouse (2015).
- [12] D. R. Ballal, A. H. Lefebvre, Ignition and flame quenching in flowing gaseous mixtures, *Proc. R. Soc. Lond. A* 357 (1977) 163–181.
- [13] C. Huang, S. Shy, C. Liu, Y. Yan, A transition on minimum ignition energy for lean turbulent methane combustion in flamelet and distributed regimes, *Proc. Combust. Inst.* 31 (2007) 1401–1409.
- [14] A. H. Lefebvre, *Gas Turbines Combustion*, Taylor & Francis, 1999.

- [15] D. R. Ballal, A. H. Lefebvre, A general model of spark ignition for gaseous and liquid fuel-air mixtures, *Symp. (Int.) Combust.* 18 (1981) 1737–1747.
- [16] D. R. Ballal, A. H. Lefebvre, Flame propagation in heterogeneous mixtures of fuel droplets, fuel vapor and air, *Symp. (Int.) Combust.* 18 (1981) 321–327.
- [17] D. R. Ballal, A. H. Lefebvre, Ignition and flame quenching of flowing heterogeneous fuel-air mixtures, *Combust. Flame* 35 (1979) 155–168.
- [18] E. S. Richardson, E. Mastorakos, Numerical investigation of forced ignition in laminar counterflow non-premixed methane-air flames, *Combust. Sci. Technol.* 179 (2007) 21–37.
- [19] N. Chakraborty, E. Mastorakos, Direct numerical simulations of localised forced ignition in turbulent mixing layers: The effects of mixture fraction and its gradient, *Flow, Turb. and Combustion* 80 (2008) 155–186.
- [20] M. Cordier, A. Vandael, G. Cabot, B. Renou, A. M. Boukhalfa, Laser-induced spark ignition of premixed confined swirled flames, *Combust. Sci. Technol.* 185 (2012) 379–407.
- [21] S. F. Ahmed, R. Balachandran, T. Marchione, E. Mastorakos, Spark ignition of turbulent nonpremixed bluff-body flames, *Combust. Flame* 151 (2007) 366–385.
- [22] T. Marchione, S. F. Ahmed, E. Mastorakos, Ignition of turbulent swirling n-heptane spray flames using single and multiple sparks, *Combust. Flame* 156 (2009) 166–180.
- [23] C. Letty, E. Mastorakos, A. R. Masri, M. Juddoo, W. O’Loughlin, Structure of igniting ethanol and n-heptane spray flames with and without swirl, *Exp. Therm. Fluid Sci.* 43 (2012) 47–54.
- [24] Q. Michalski, C. J. Benito-Parejo, A. Claverie, J. Sotton, M. Bellenoue, An application of speckle-based background oriented schlieren for optical calorimetry, *Exp. Therm. Fluid Sci.* 91 (2018) 470–478.

- [25] J. Hirschfelder, C. Curtis, B. Bird, *Molecular Theory of Gases and Liquids*, John Wiley & Sons, 1954.
- [26] T. Jaravel, Prediction of pollutants in gas turbines using large eddy simulation, Ph.D. thesis, Institut National Polytechnique de Toulouse (2016).
- [27] F. Nicoud, H. Toda, O. Cabrit, S. Bose, J. Lee, Using singular values to build a subgrid-scale model for large eddy simulations, *Phys. Fluids* 8 (2011) 085106.
- [28] B. Rochette, B. Cuenot, E. Riber, O. Vermorel, A generic and self-adapting method for flame detection and thickening in the thickened flame model, *Combust. Flame* 212 (2019) 448–458.
- [29] O. Colin, F. Ducros, D. Veynante, T. Poinso, A thickened flame model for large eddy simulations of turbulent premixed combustion, *Phys. Fluids* 12 (2000) 1843–1863.
- [30] F. Charlette, D. Veynante, C. Meneveau, A power-law wrinkling model for LES of premixed turbulent combustion: Part I - non-dynamic formulation and initial tests, *Combust. Flame* 131 (2002) 159–180.
- [31] S. Puggelli, D. Veynante, R. Vicquelin, Impact of dynamic modelling of the flame subgrid scale wrinkling in large-Eddy simulation of light-round in an annular combustor, *Combust. Flame* 230 (2021) 166–178.
- [32] P. S. Volpiani, T. Schmitt, D. Veynante, Large eddy simulation of a turbulent swirling premixed flame coupling the TFLES model with a dynamic wrinkling formulation, *Combust. Flame* 180 (2017) 124–135.
- [33] F. Charlette, D. Veynante, C. Meneveau, A power-law flame wrinkling model for LES of premixed turbulent combustion part II: Dynamic formulation, *Combust. Flame* 131 (2002) 181–197.
- [34] M. Boileau, Simulation aux grandes échelles de l’allumage diphasique des foyers aéronautiques, PhD thesis, Institut National Polytechnique de Toulouse (2007).
- [35] T. Lu, C. Law, A criterion based on computational singular perturbation for the identification of quasi steady state species., *Combust. Flame* 154 (2008) 763–774.

- [36] P. Pouech, F. Duchaine, T. Poinso, Premixed flame ignition in high-speed flows over a backward facing step, *Combust. Flame* 229 (2021) 111398.
- [37] E. Ranzi, A. Frassoldati, R. Grana, A. Cuoci, T. Faravelli, A. P. Kelley, C. K. Law, Hierarchical and comparative kinetic modeling of laminar flame speeds of hydrocarbon and oxygenated fuels, *Prog. Energy Comb. Sci.* 38 (2012) 468–501.
- [38] B. Franzelli, Impact of the chemical description on direct numerical simulations and large eddy simulations of turbulent combustion in industrial aero-engines, Ph.D. thesis, Institut National Polytechnique de Toulouse (2011).
- [39] G. Lacaze, E. Richardson, T. J. Poinso, Large eddy simulation of spark ignition in a turbulent methane jet, *Combust. Flame* 156 (2009) 1993–2009.
- [40] B. McBride, S. Gordon, M. Reno, Coefficients for calculating thermodynamic and transport properties of individual species, Tech. Rep. TM-4513, NASA (1994).

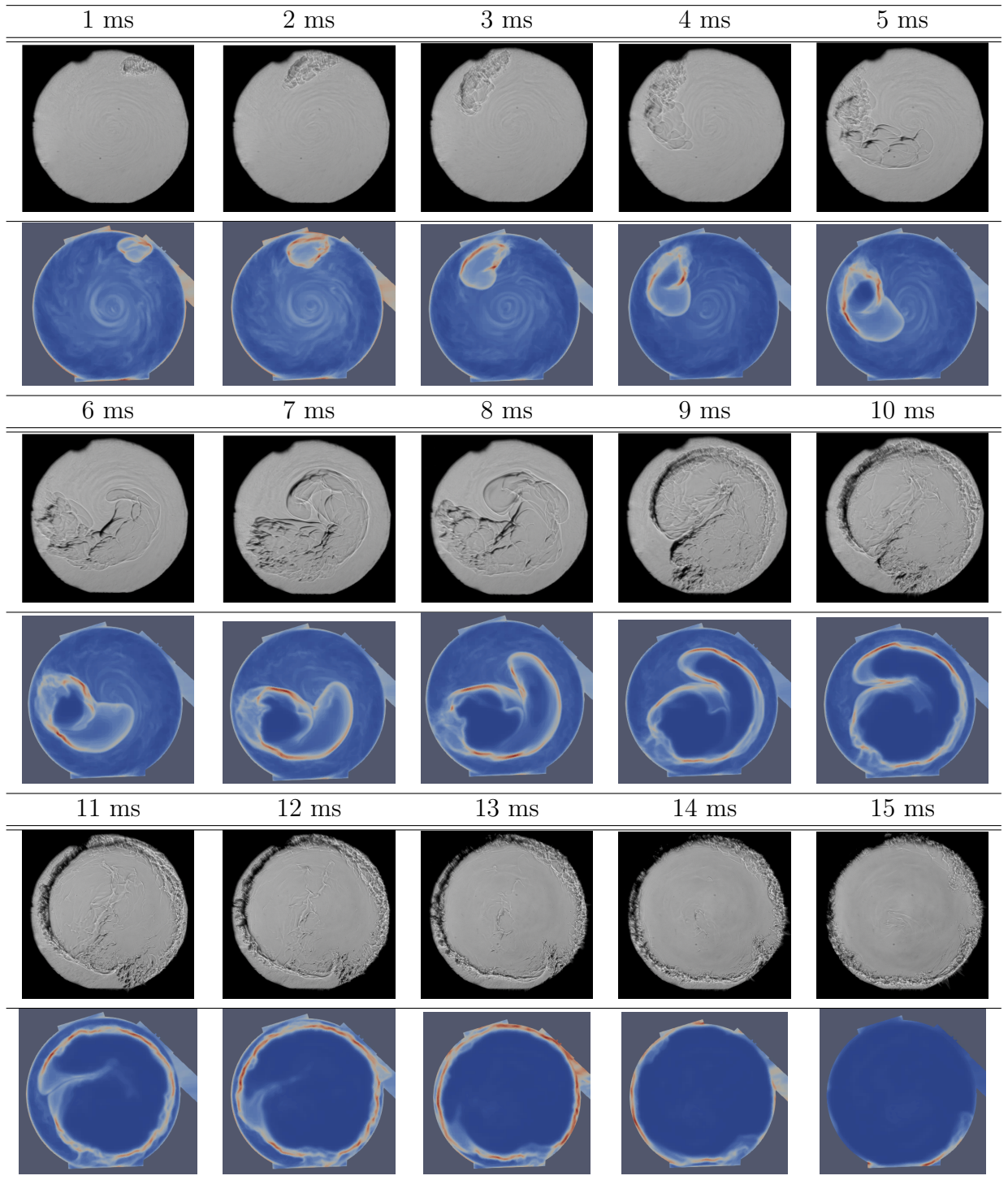
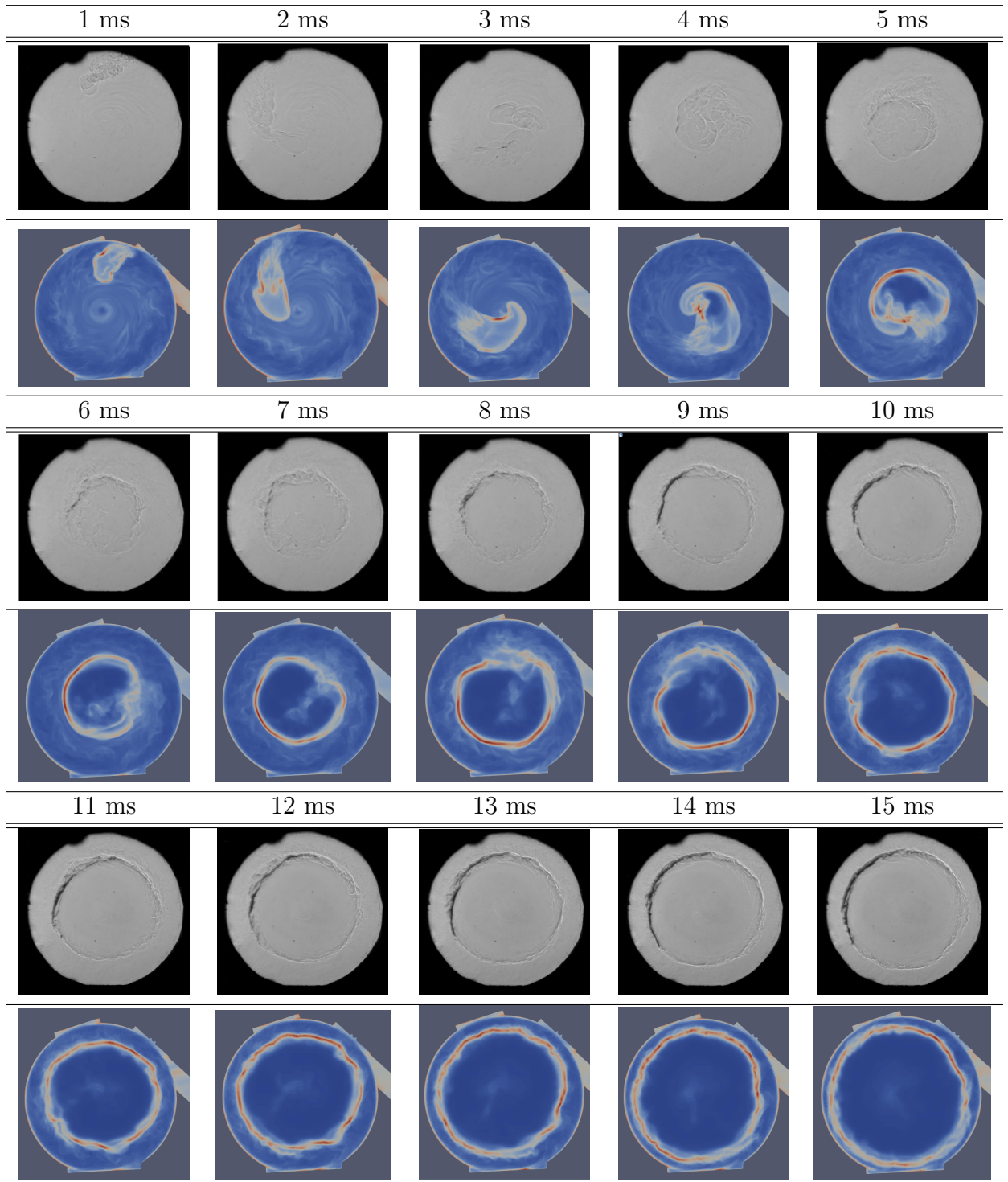


Figure A.1: Comparison of Schlieren images with LOS integrated density gradient images from LES for case A ($p_{ini} = 1\text{bar}$, $t_{delay} = 5\text{ms}$) at various times after spark. Static efficiency formulation



41

Figure A.2: Comparison of Schlieren images with LOS integrated density gradient images from LES for case B ($p_{ini} = 0.5\text{bar}$, $t_{delay} = 5\text{ms}$) at various times after spark. Static efficiency formulation

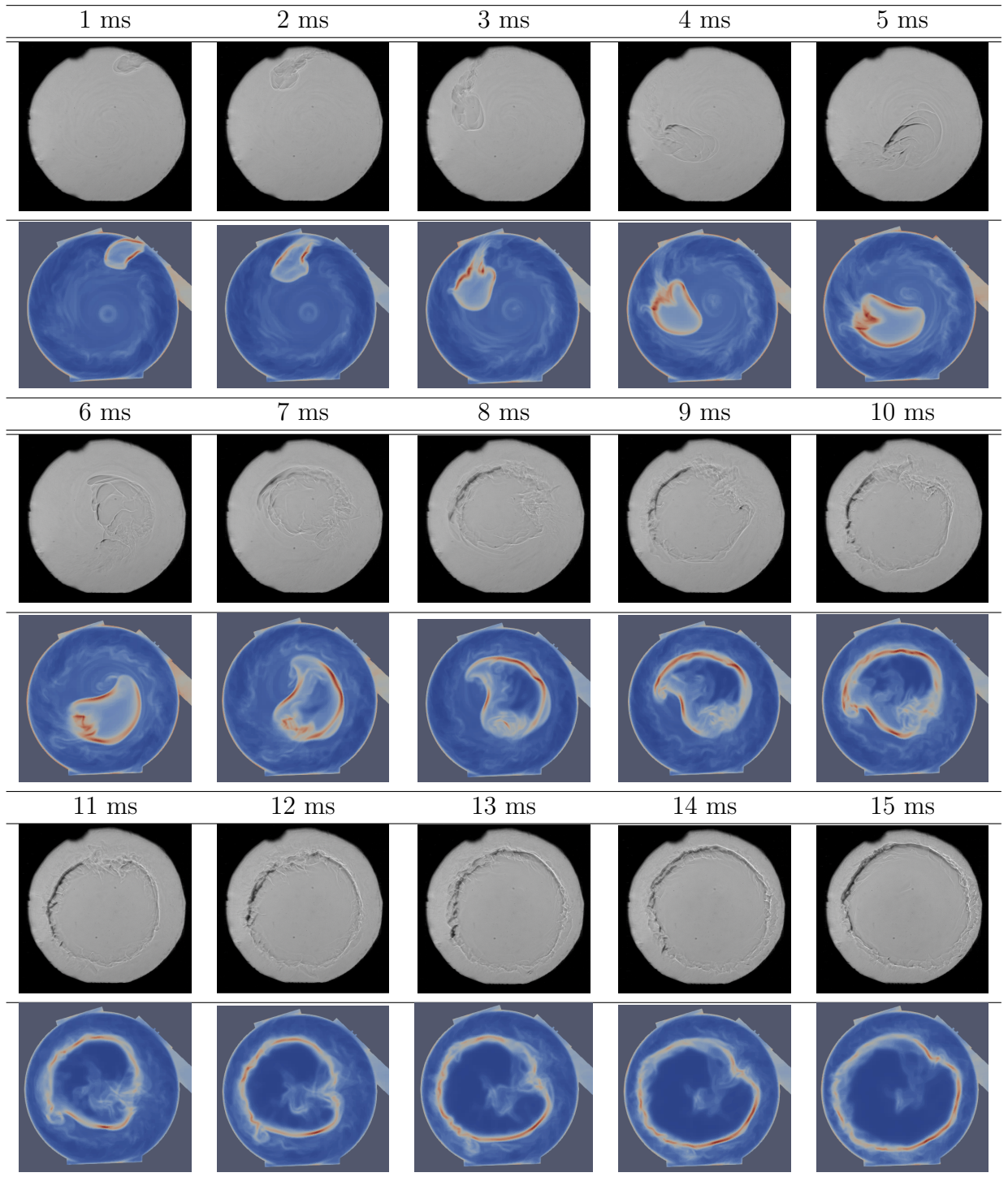


Figure A.3: Comparison of Schlieren images with LOS integrated density gradient images from LES for case C ($p_{ini} = 0.5\text{bar}$, $t_{delay} = 30\text{ms}$) at various times after spark. Static efficiency formulation

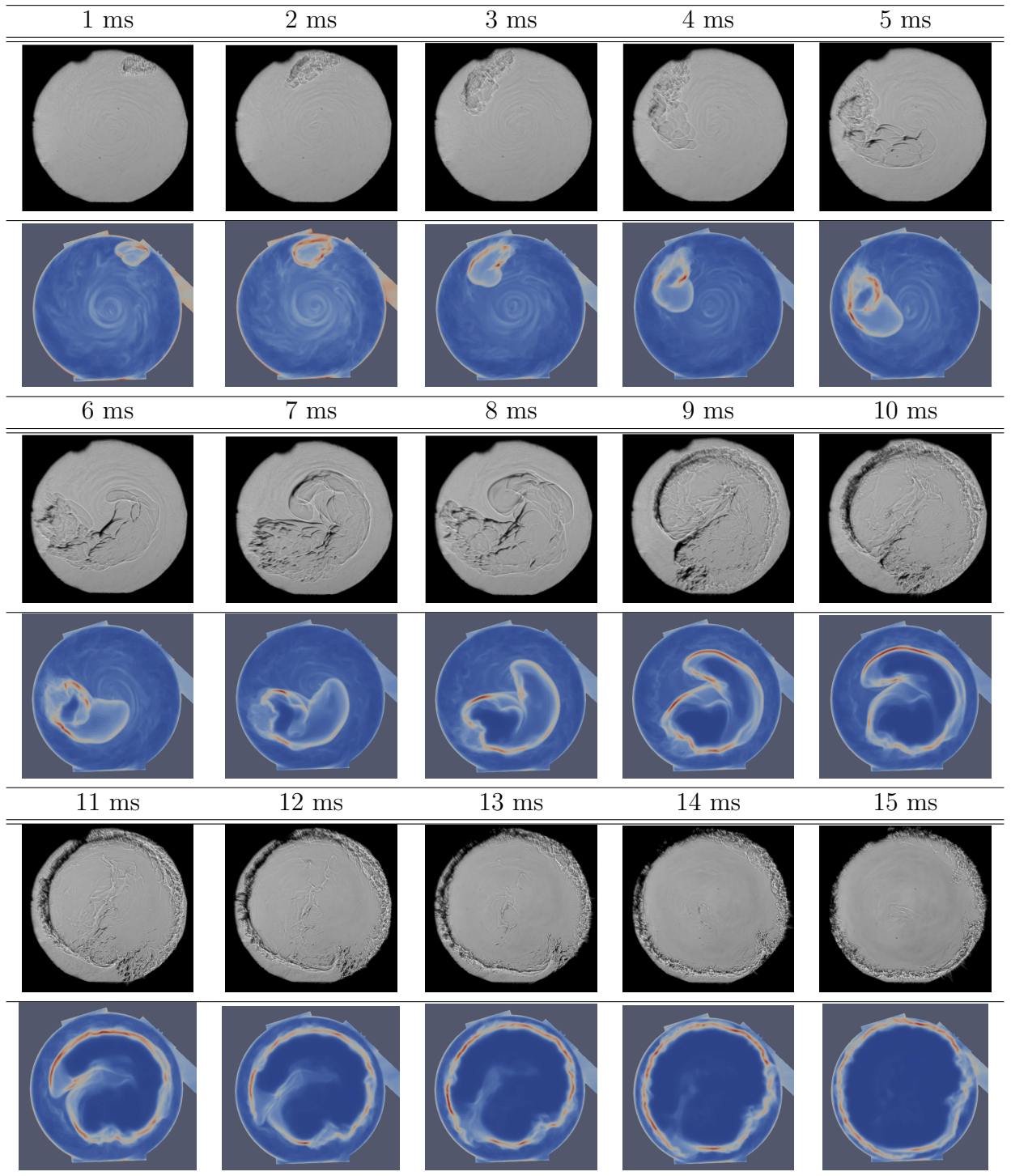


Figure A.4: Comparison of Schlieren images with LOS integrated density gradient images from LES for case A ($p_{ini} = 1\text{bar}$, $t_{delay} = 5\text{ms}$) at various times after spark. Dynamic efficiency formulation

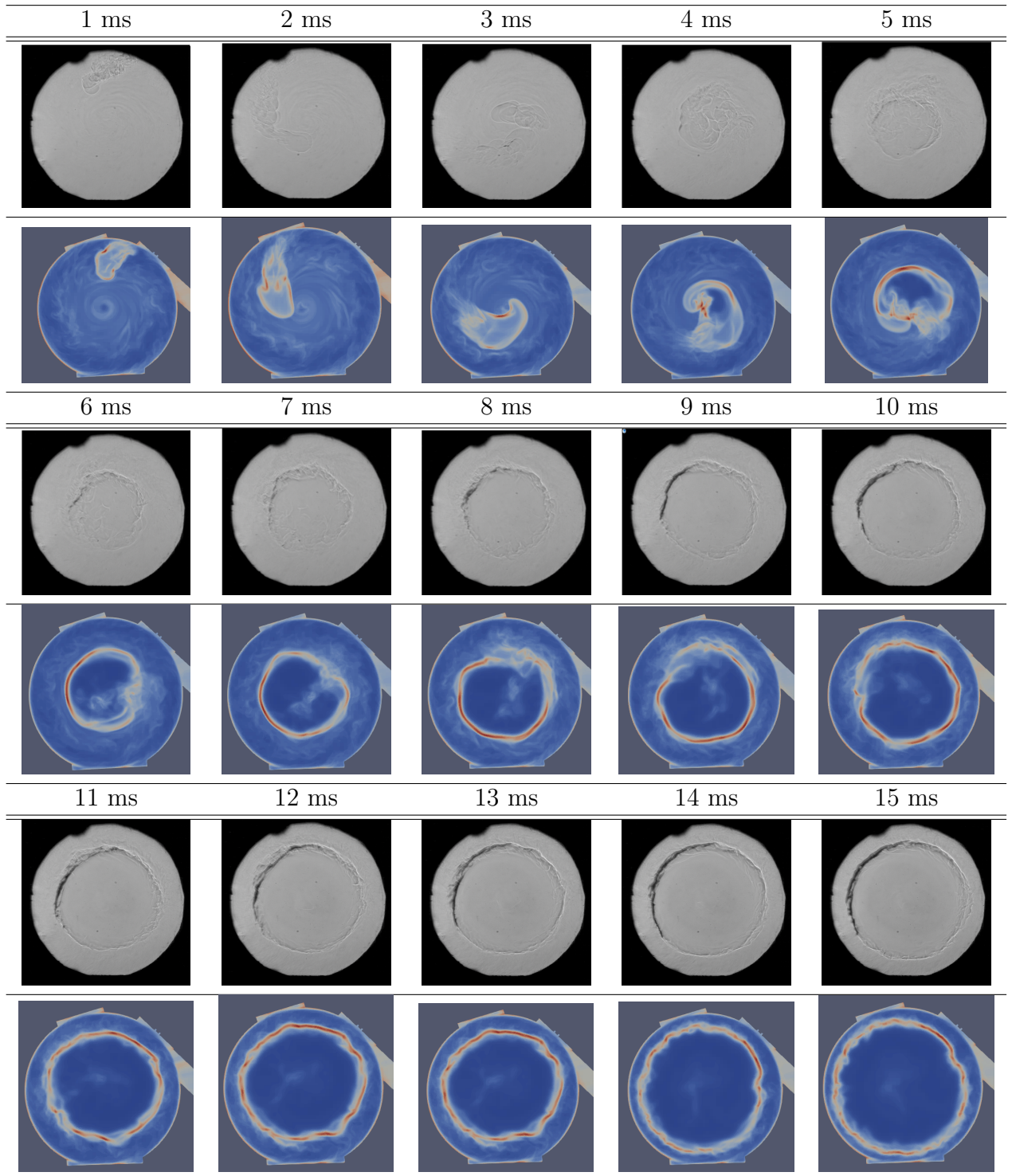


Figure A.5: Comparison of Schlieren images with LOS integrated density gradient images from LES for case B ($p_{ini} = 0.5\text{bar}$, $t_{delay} = 5\text{ms}$) at various times after spark. Dynamic efficiency formulation

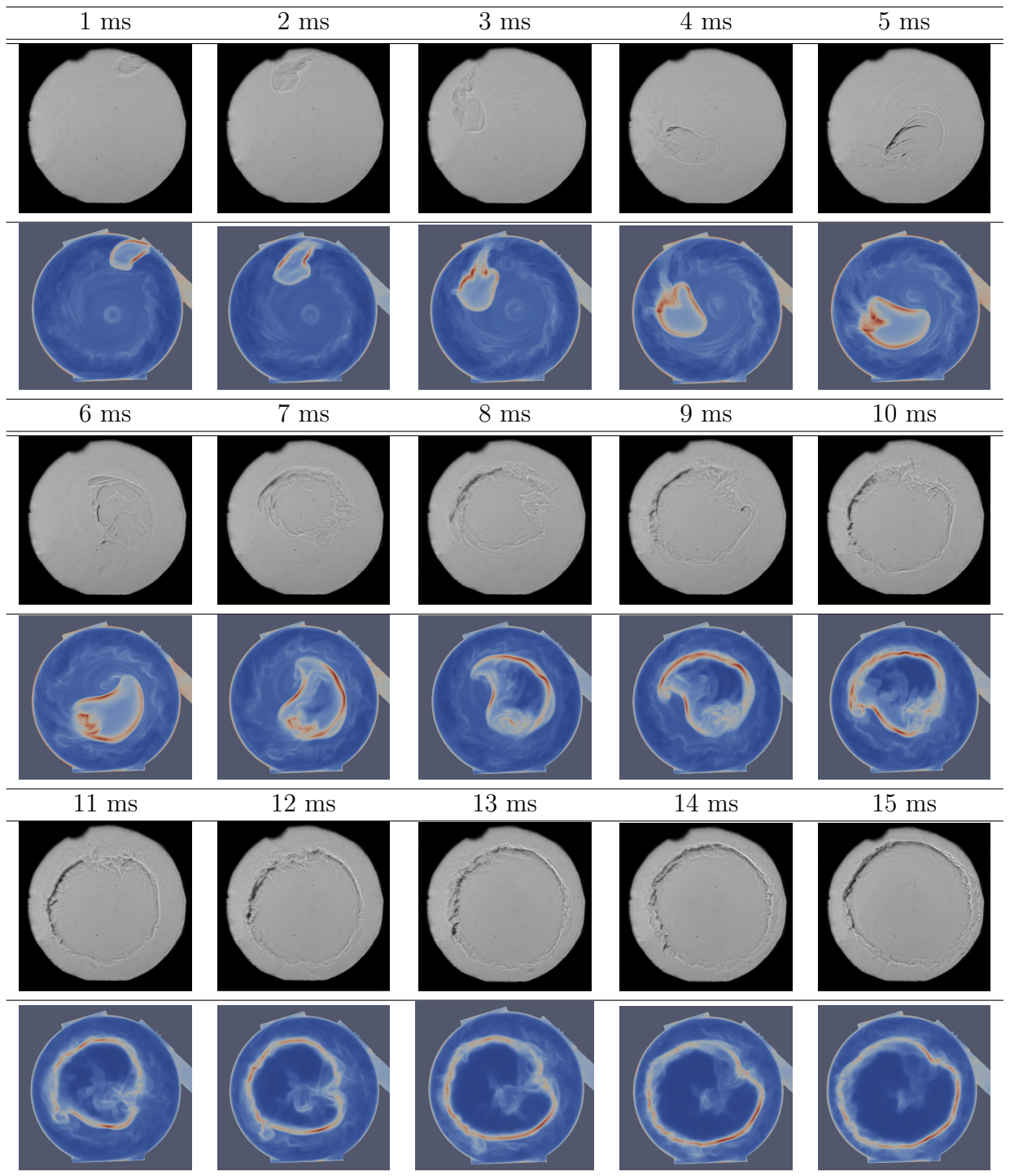


Figure A.6: Comparison of Schlieren images with LOS integrated density gradient images from LES for case C ($p_{ini} = 0.5\text{bar}$, $t_{delay} = 30\text{ms}$) at various times after spark. Dynamic efficiency formulation

Figure A.7: Evolution of β PDF for an isosurface of $q=0.5$, Case A ($p_{ini} = 1bar$, $t_{delay} = 5ms$) for various times after spark

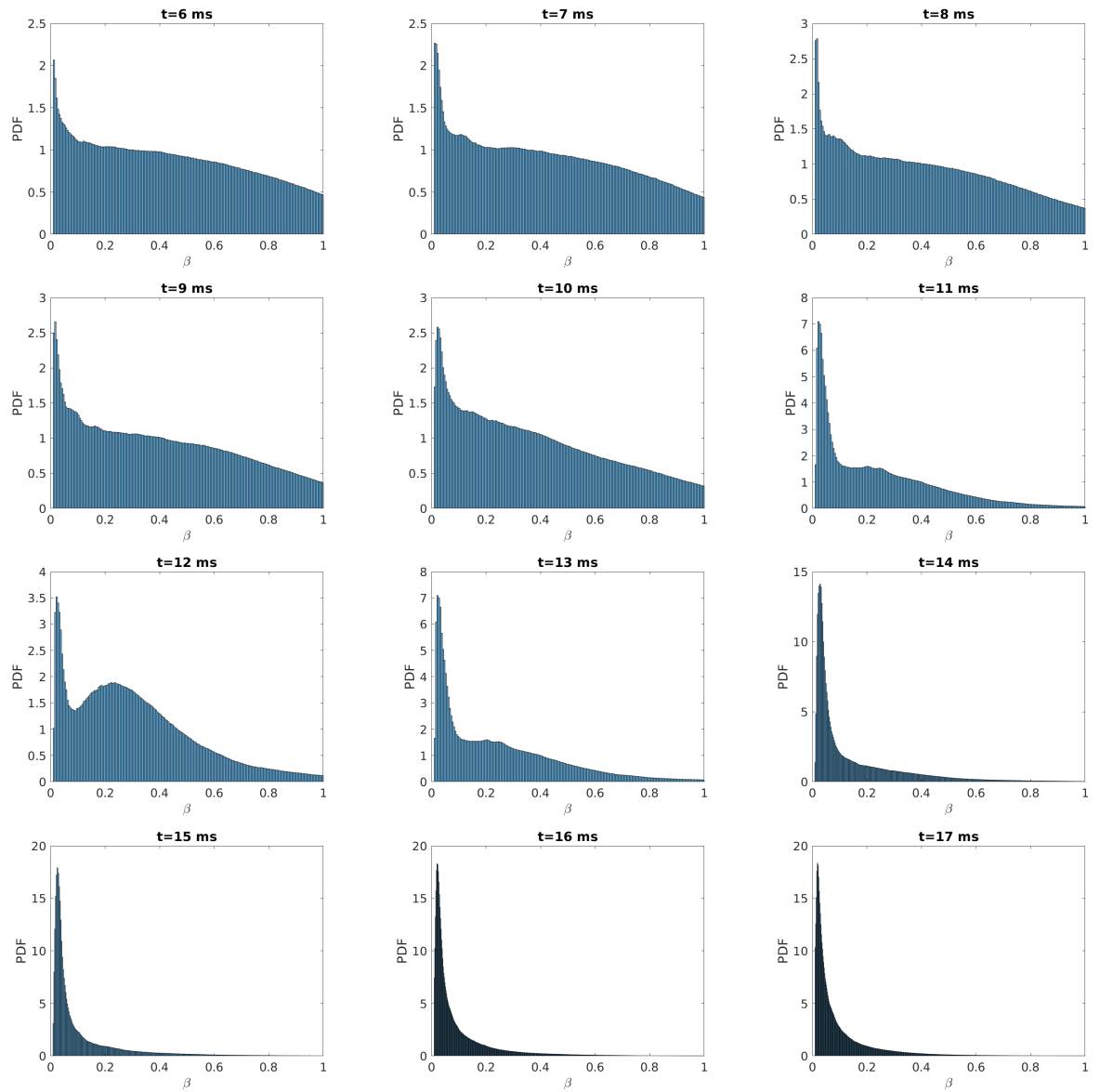


Figure A.8: Evolution of β PDF for an isosurface of $q=0.5$, Case B ($p_{ini} = 0.5\text{bar}$, $t_{delay} = 5\text{ms}$) for various times after spark

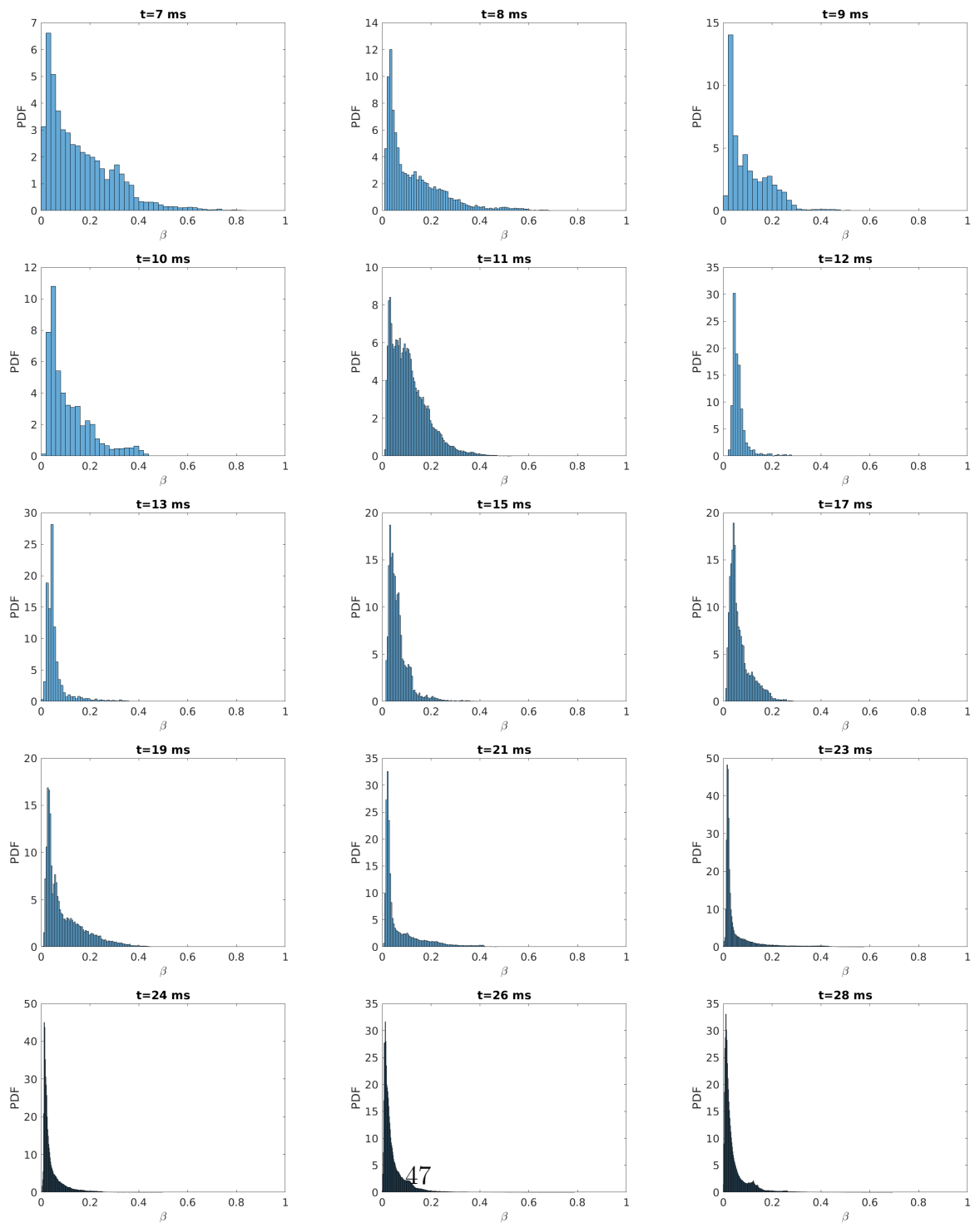


Figure A.9: Evolution of β PDF for an isosurface of $q=0.5$, Case C ($p_{ini} = 0.5bar$, $t_{delay} = 30ms$) for various times after spark

